RICE UNIVERSITY

Centrifugally Driven Radial Convection of Plasma in Saturn's Inner Magnetosphere

By

Yi Chen

A THESIS SUBMITTED
IN PARTIAL FULFILLMENT OF THE
REQUIREMENTS FOR THE DEGREE

Doctor of Philosophy

APPROVED, THESIS COMMITTEE:

Thomas W. Hill, Professor,
Department of Physics and Astronomy
Chair of Thesis Committee

Patricia H. Reiff, Professor,
Department of Physics and Astronomy

Stephen Semmes, Noah Harding Professor,
Department of Mathematics

HOUSTON, TEXAS
OCTOBER 2010

ABSTRACT

Centrifugally Driven Radial Convection of Plasma in Saturn's Inner Magnetosphere

By

Yi Chen

Theoretical studies have pointed out that in the inner part of a rapidly rotating magnetosphere such as that of Jupiter and Saturn, the dominant driving factor of radial plasma transport is the centrifugal interchange instability. After the in-situ observations of the Cassini spacecraft became available, the major observable signature of radial plasma convection is reported as a series of longitudinally localized injections and simultaneous drift dispersions of hot tenuous plasma from the outer magnetosphere. The Cassini Plasma Spectrometer (CAPS) and the Cassini Magnetospheric Imaging Instrument (MIMI) have observed signatures of these processes frequently, providing direct evidence for Saturn's magnetospheric centrifugally driven convective motions, in which the radial transport of plasma comprises hot, tenuous plasma moving inward and cooler, denser plasma moving outward.

With methods similar to those of *Hill et al.* [2005], we study the statistics of the properties of such events by analyzing CAPS data from 26 Cassini orbits. A statistical picture of their major characteristics is developed, including the distributions of ages,

longitudinal widths, radial distances, and longitudes and local times, which are all consistent with previous results. An unexpected longitude modulation of these events appears in the old (SLS) longitude system, while no such modulation seems to exist in the new (SLS2/SLS3) longitude system. A Lomb periodogram analysis, however, reveals no significant periodic modulation of these events.

We further extend the statistical sample of these injection/dispersion events and find that the inflow channels occupy only a small fraction (~ 7%) of the total available longitudinal space, indicating that the inflow sectors are much narrower than the outflow sectors. Furthermore, we assume that the plasma is largely confined to a thin equatorial sheet, and calculate its thickness by deriving the centrifugal scale height profile based on the CAPS observations. We also present the radial and longitudinal dependences of flux tube mass content, as well as the total ion mass between 5 and 10 Saturn radii. Combining these results, we estimate a global plasma mass outflow rate ~ 280 kg/s.

Acknowledgements

I would like to express my deepest gratitude to my thesis advisor, Professor Thomas W. Hill, for his invaluable guidance and encouragement throughout this work. He always provides me with enlightening ideas and constructive suggestions, and inspires me with his remarkable expertise and extensive knowledge background.

I am grateful to all the scientists and technicians on the Cassini Plasma Spectrometer (CAPS) team for providing not only the excellent scientific data, but also a great teamwork environment. Special recognitions go to Dr. Abi Rymer and Dr. Rob Wilson for their helpful suggestions and informative discussions. I would like to acknowledge in particular Mr. Prachet (Pat) Mokashi for giving me introductions of the CAPS data system at the very beginning of my research work at Rice.

Many thanks go to Professor Pat Reiff and Professor Stephen Semmes, for contributing their precious time as the committee members for this thesis work. I would also like to thank other faculty members and fellow graduate students in our group for helpful discussions and suggestions.

This thesis is dedicated to my family – my wife Lisha Xie, my parents Lanhua Wu and Longtang Chen. I would never get it done without their love and support.

Table of Contents

1. Introduction

1.1. Magnetospheres in the solar system

A planetary magnetosphere is a broad region of space around the planet formed because of the interaction between its intrinsic magnetic field and the solar wind, which is the fast stream of magnetized energetic charged particles originating from the Sun's upper atmosphere. Dominated by the magnetic field, the magnetosphere creates a shield for the planet, and thus acts as an obstacle for the supersonic solar wind flows. Besides the magnetic field, the complicated system of the magnetosphere usually also comprises electric fields, plasmas, and energetic particles.

It is known that of the eight planets, six are enveloped by their own magnetospheres (Mercury, Earth, Jupiter, Saturn, Uranus, and Neptune). Venus and Mars don't have strong enough intrinsic magnetic moments to form their own magnetospheres; instead, the solar wind interacts directly with their ionospheres. This kind of interaction produces an "induced" magnetosphere. Besides those six planets, Jupiter's moon, Ganymede, is the only known planetary satellite in the solar system that has a sufficient intrinsic magnetic field to form its own magnetosphere within the much larger Jovian magnetosphere.

1.2. Earth's magnetosphere

The Earth's magnetosphere is by far the first and the most studied, therefore the best understood, of the six planetary magnetospheres in the solar system. Figure 1.1 shows the basic structure of the Earth's magnetosphere in the noon-midnight meridian plane. It is clear that the solar wind compresses the Earth's magnetic field on the day side and stretches it on the night side into a long magnetotail, thus generating the basic comet-shaped cavity of the terrestrial magnetosphere. A shock wave, named the bow shock, is formed on the day side to slow and deflect the supersonic solar wind around the obstacle. The solar wind particles that pass through the bow shock slow down to subsonic speeds and form the region of space named the magnetosheath. The boundary separating the terrestrial field in the magnetosphere and the interplanetary magnetic field (IMF) in the magnetosheath is called the magnetopause. Inside the magnetopause, the motion of a charged particle in the magnetosphere is dominated by the planet's magnetic field. Other important features of Earth's magnetosphere include the Van Allen radiation belts, which consist of energetic charged particles that move along the field lines and oscillate back and forth between southern and northern hemispheres, and the plasma sheet, which is located in the central region of the magnetotail near the magnetic equatorial plane and separates open field lines with different directions.

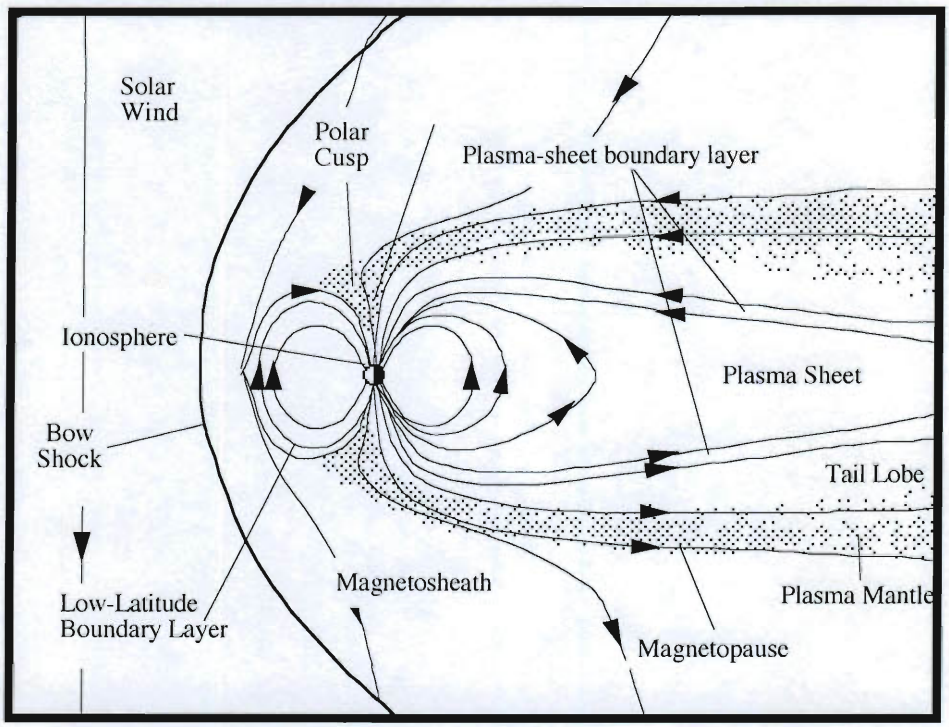

Figure 1.1. Sketch of plasma regions in the space around the Earth, viewed in the noon-midnight meridian plane. The Sun is on the left. The interplanetary field is pointing southward in this picture. This figure is from *Wolf* [1995].

1.3. Saturn's magnetosphere

Saturn is the second largest planet after Jupiter, and the sixth one in distance from the sun. It belongs to the "gas giant" category together with Jupiter, Uranus and Neptune. Saturn's equatorial radius is about 60,268 km, and its rotation period is about 10.8 hours. Perhaps the most visually remarkable feature of Saturn is its spectacular ring system. Meanwhile, Saturn has dozens of natural satellites, including several icy satellites that are enveloped in the magnetosphere. Saturn's largest satellite, Titan, is famous for having a dense atmosphere consisting mainly of methane and nitrogen.

Saturn's magnetic axis is almost perfectly aligned with the planet's rotation axis. The equatorial surface field strength is about 0.21 *Gauss*. Like Jupiter's magnetic field, its polarity is opposite to that of the Earth, i.e., directed from north to south. Although the equatorial ring current system brings significant distortion to the dipole field in the middle and outer magnetosphere, it is often treated as a pure dipole in the inner magnetosphere in theoretical studies.

Consistent with the size of the planet itself, Saturn's magnetosphere is the second largest one in the solar system, smaller only than that of Jupiter. It has a basic comet-like shape (Figure 1.2) like all the other planetary magnetospheres, with a bow shock at around 30 Saturn radii on the day side and an elongated tail structure on the night side probably extending to hundreds of Saturn radii downstream.

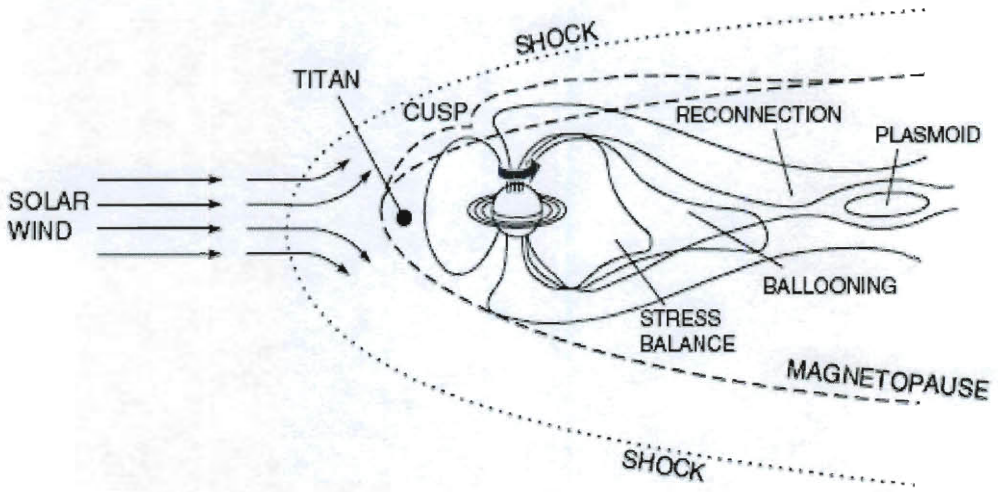

Figure 1.2. Basic structure of Saturn's magnetosphere. In this picture, Titan is located just inside the magnetopause. Figure from *Dougherty* [2001].

Unlike other planetary magnetospheres, Saturn's magnetosphere envelops an extensive ring system and a collection of small icy satellites. Titan, which is located at about 20 R_S from Saturn, can also be enclosed inside the magnetopause depending on the solar wind conditions. These rings and satellites provide important sources and sinks for plasma, which in turn can affect the evolution of the rings and the satellites' surfaces. The sketch in Figure 1.3 qualitatively shows the E-ring mass density distribution in the meridian plane, as well as the locations of Saturn's major satellites.

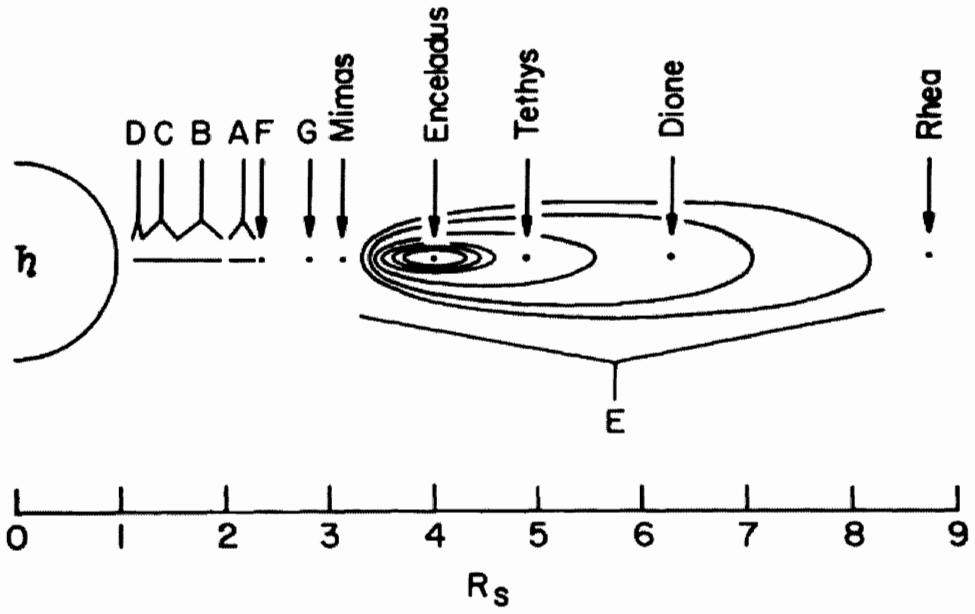

Figure 1.3. Sketch of the E-ring mass density distribution in a meridian plane. This figure shows clearly the radial distances of various rings and icy satellites. Figure from *Hill* [1984].

Using plasma data measured by the Cassini Plasma Spectrometer (CAPS), which we will introduce in detail later, *Young et al.* [2005] initiated the systematic investigation of Saturn's magnetospheric plasma properties and chemical composition that continues to this day. Just inside the magnetopause (~ 20 R_S near the noon meridian), the "outer magnetosphere" contains mainly hot tenuous plasma, sometimes dominated by H^+. Inside of about 15 R_S, the plasma population is dominated by cooler, denser plasma of internal origin, as indicated by its ion composition, dominated by "water-group" ions (designated W^+) including O^+, OH^+, H_2O^+, and H_3O^+. The innermost region is located directly over the A and B rings (~ 2 R_S), and consists primarily of O^+ and O_2^+. This thesis focuses on the region of Saturn's "inner magnetosphere" (~5 – 10 R_S), where the dominant species of ions are the water-group ions.

1.4. Dynamics of planetary magnetospheres

Our study deals with problems associated with dynamic processes in Saturn's magnetosphere, so it is appropriate to introduce here the fundamental theories that have been developed to describe the dynamics of planetary magnetospheres. There are two basically different types of mechanism to drive convection (plasma motion) in planetary magnetospheres: the solar-wind-driven dynamics represented by the Earth's magnetosphere, and the rotation-driven dynamics that takes place in Jupiter's and Saturn's magnetospheres.

1.4.1. Solar-wind-driven magnetospheric convection

The major energy and particle source for the Earth's magnetosphere is now known to be the solar wind, which provides sufficient energy input to trigger many forms of geomagnetic activity including two basic modes of magnetospheric convection: the magnetic storm and the magnetospheric substorm.

Dungey (1961) proposed an open model for the Earth's magnetosphere, where magnetic reconnection plays a key role in its coupling with the solar wind. It is now clear that this open model can explain the basic convection process in the terrestrial magnetosphere. Figure 1.4 illustrates the qualitative plasma flow pattern of Dungey's model, shown in the noon-midnight meridian plane. When the IMF direction turns southward just outside the day side magnetopause, the antiparallel field lines of the IMF and terrestrial field merge together, so that the topology of magnetic fields at the magnetosphere's boundary changes dramatically. This process is named magnetic reconnection, and also takes place in the magnetotail. These locations are indicated in the figure by the X-shaped lines. These X-lines represent surfaces that separate regions containing topologically different (i.e., closed or open) magnetic field lines.

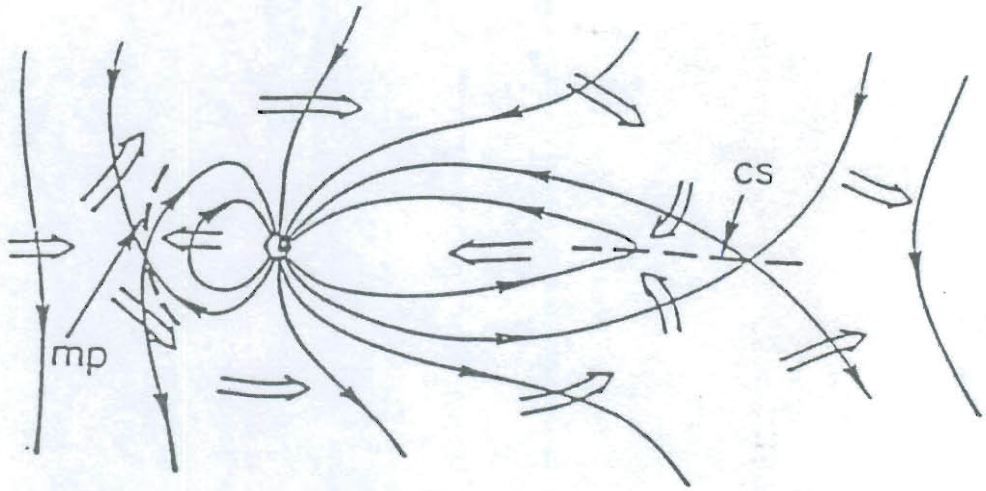

Figure 1.4. Sketch of Dungey's open model of the magnetosphere, shown in the noon-midnight meridian plane. Note that the IMF is pointing southward in this figure. This figure is from *Hill* [1983].

After magnetic reconnection takes place at the day side, the solar wind can flow across the magnetopause to enter the magnetosphere, transmitting both energy and particles, and driving the flow pattern indicated by the large arrows in Figure 1.4 on open field lines that connect the solar wind directly to the Earth's polar caps. Subsequent reconnection on the night side then causes a sudden release of energy in the magnetotail and charged particle injections toward the Earth to generate auroral expansions and other aspects of magnetospheric substorms. A substorm typically lasts for about 1 to 2 hours.

Another large-scale dynamic process, the geomagnetic storm, is also driven by the open-model process of magnetic reconnection, and is characterized by a systematic decrease of the northward geomagnetic field at low latitudes on the Earth's surface. This main phase of a magnetic storm usually lasts several hours, during which one or more substorms may occur. After the main phase, it can take several days for the magnetic field to recover to its normal state.

The Earth's magnetosphere also contains a complex current system that is composed of several different kinds of large-scale currents. Figure 1.5 shows a sketch of major types of currents observed from a view slightly above the magnetic equatorial plane. These currents are carried by charged particles in different regions of the magnetosphere, and play important roles in the magnetospheric convection system. For example, the field-aligned Birkeland currents connect the partial ring current in the tail region with ionospheric currents, thus transferring momentum and energy

between the ionosphere and magnetosphere. The Chapman-Ferraro current on the magnetopause forms the boundary between the magnetosheath and the magnetosphere. The westward ring current in the inner magnetosphere produces perturbations to the dipole field that are amplified during geomagnetic storms. The tail current in the magnetotail also flows westward, and separates the oppositely-directed fields on either side of the plasma sheet.

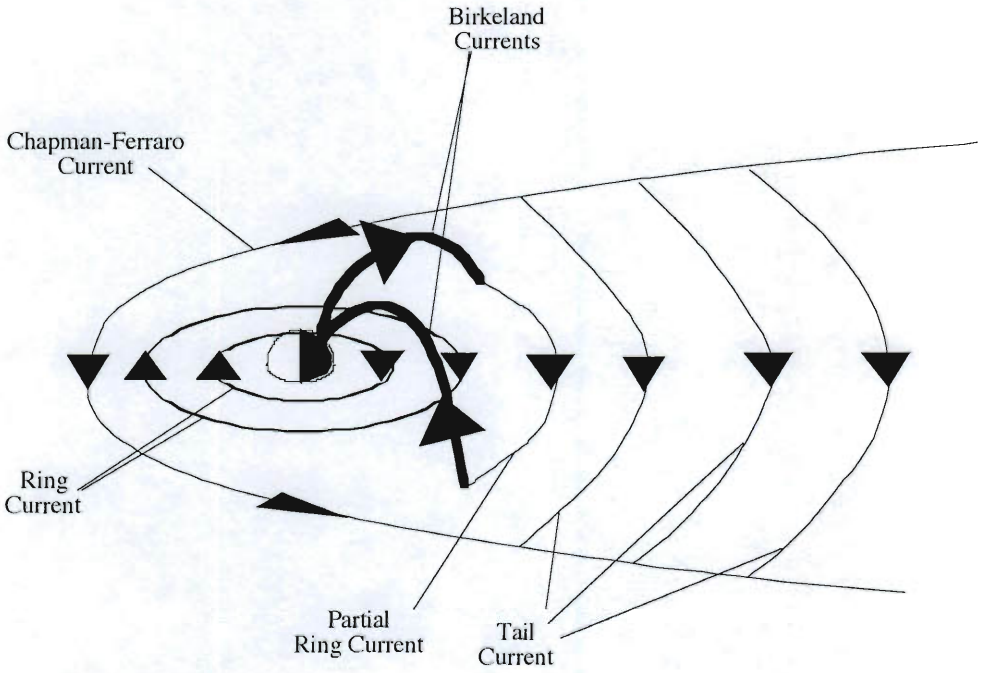

Figure 1.5. Sketch of the current systems in Earth's magnetosphere, viewed from slightly above the magnetic equatorial plane. Figure from *Wolf* [1995].

1.4.2. Rotation-driven magnetospheric convection

Jupiter's and Saturn's magnetospheres have different configurations and dynamics from Earth's because their convection systems are dominated by rotational effects. *Brice and Ioannidis* [1970] argued that in a given magnetosphere, a competition always exists between solar-wind driven convection and rotationally driven convection. The competition of these two mechanisms defines a physical boundary, named the plasmapause, where the magnetospheric convection pattern changes from rotationally driven inside of this boundary to solar-wind driven outside of it [*Hill and Dessler,* 1991]. For Earth, the average plasmapause radius is ~ 6 R_E, about half the distance to the day side magnetopause. For Jupiter and Saturn, the scaled plasmapause radii are ~ 260 R_J and ~68 R_S, while their day side magnetopauses are located at ~ 50-75 R_J and ~ 20 R_S, respectively [*Mauk et al.,* 2009]. Therefore, both Jupiter's and Saturn's magnetospheres are well inside their theoretical plasmapause radii, indicating that their convection systems should be dominated by the centrifugal force due to corotation with the planet.

Another key feature of an outer planet's magnetosphere is that it comes with a dominant internal plasma source. In Jupiter's inner magnetosphere, the volcanic satellite Io ejects sulfur and sulfur dioxide particles that become ionized to form a plasma torus near the orbit of Io (~ 5.9 R_J) [*Hill et al.*, 1983]. In Saturn's case, the major plasma source is now known to be the neutral torus produced by the icy satellite Enceladus [e.g., *Johnson et al.,* 2006; *Pontius and Hill,* 2009], which has an

orbital distance of 3.96 R_S. Shortly after arriving in Saturn orbit, Cassini observed a prominent plume being ejected from Enceladus' south pole region, which was recognized as frozen water ice particles streaming outward into space [*Porco et al.*, 2006]. The visible ice plumes are accompanied by jets of neutral water molecules [*Waite et al.*, 2006] which, unlike the Io volcanic ejecta at Jupiter, are scattered and spread out from Enceladus' orbit before being ionized at greater distances [*Johnson et al.,* 2006]. In both cases, the centrifugal force is much larger than gravity at the locations of the plasma sources, making the local net force outward. Therefore, the newly generated plasma is transported outward to the outer magnetosphere where it is lost, to maintain a steady-state magnetospheric mass content.

Vasyliūnas [1983] proposed a rotationally driven flow pattern for the Jovian magnetosphere, where plasma is lost ultimately in the form of plasmoids in the magnetotail, forming a down-tail planetary wind [*Hill et al.*, 1983] through magnetic reconnection. Figure 1.6 is a schematic illustration of this flow pattern in the equatorial plane, and resulting magnetic configurations in successive meridian surfaces, which illustrates clearly that the centrifugal force plays an important role in driving such plasma flows. This same basic pattern has been widely adopted in interpretations of Cassini observations at Saturn.

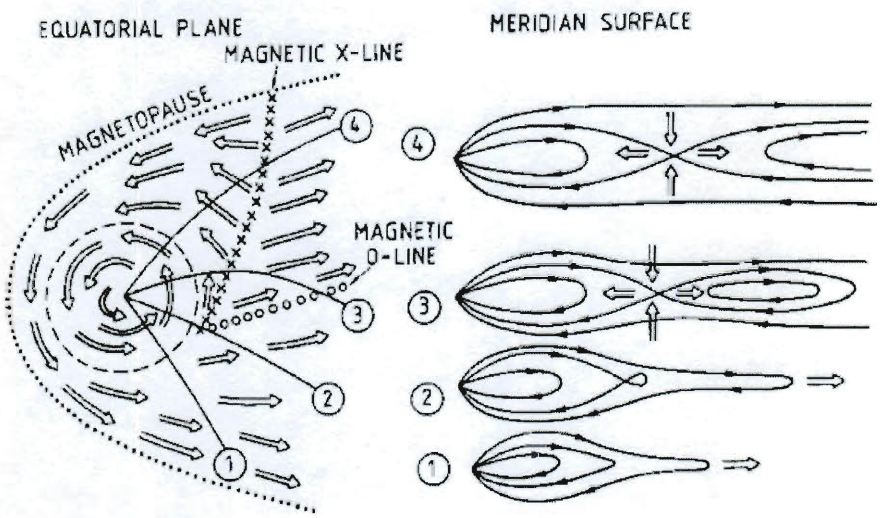

Figure 1.6. Sketch of plasma flow in Jupiter's equatorial plane (left) and the associated plasma flow and magnetic field configurations in a sequence of meridian surfaces (right), proposed by *Vasyliūnas* [1983].

Like Earth's magnetosphere, the magnetospheres of the outer planets also have their own characteristic current systems. But unlike Earth's magnetosphere, whose current systems are largely associated with the interaction between the solar wind and the magnetosphere, the current systems of the outer planets are largely induced internally by rotational effects. In particular, the ring current exists, at least in part, to balance the centrifugal force of (partial) corotation. Any longitudinal asymmetry of the magnetospheric plasma mass density produces a partial ring current in the azimuthal direction, which requires closure in the ionosphere via Birkeland currents, as shown in Figure 1.7. A different Birkeland current system, illustrated in Figure 1.8, transmits planetary angular momentum outward to enforce partial corotation between the magnetosphere and the planet [*Hill*, 1979]. The radial, near-equatorial part of this current circuit provides the spin-up $\mathbf{J}\times\mathbf{B}$ torque to maintain partial corotation of newly-created plasma (the "pick-up current") and of outwardly transported plasma (the "Coriolis current").

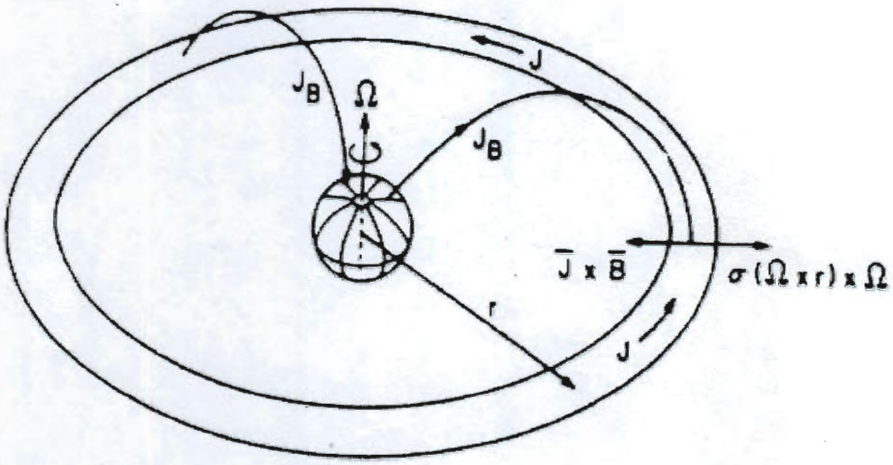

Figure 1.7. Schematic illustration of a Birkeland current system that includes a partial ring current, proposed for Jupiter's magnetosphere by *Dessler* [1980].

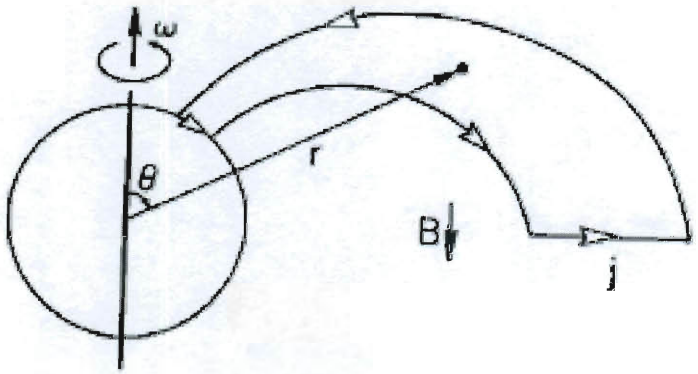

Figure 1.8. Rotationally-induced Birkeland current system in the meridian plane that is responsible for outward transport of angular momentum. This figure is from *Hill* [1979].

Observations by the Cassini spacecraft have provided direct evidence to support the picture of rotationally driven magnetospheric convection at Saturn. The primary topic of this thesis is the processes of plasma radial transport in Saturn's inner magnetosphere as revealed by CAPS observations.

2. Theories of rotation-driven magnetospheric convection

We have stated above that in the magnetospheric convection process at Saturn, the dominant driving force is the centrifugal force caused by the planet's fast rotation. New plasma is generated in the inner part of the magnetosphere and needs to be transported to outer regions of the magnetosphere, so that a steady-state distribution of mass content can be maintained. How does this outward transport take place? We have briefly introduced the Vasyliūnas dynamic cycle in Section 1.4.2 (Figure 1.6). In this chapter, we further discuss previous theoretical efforts to describe the plasma transport processes. In particular, models that are based on the centrifugal interchange instability are introduced as part of the basic motivation of our observational study.

2.1. Concept of interchange instability

In plasma physics, the interchange instability can be viewed as a generalization of the Rayleigh-Taylor instability in hydrodynamics. Consider a tank filled with two different kinds of fluids, as shown in Figure 2.1. If a denser fluid is suspended above a less dense fluid, the system is unstable because its total gravitational potential energy can be reduced by interchanging the two fluids. Given a small perturbation at the boundary, the denser fluid tends to move down under the influence of gravity, and switches places with the less-dense fluid that tends to move up, such that the potential energy of the system decreases to a minimum. The two fluids interchange places after this process, just as the name "interchange instability" implies.

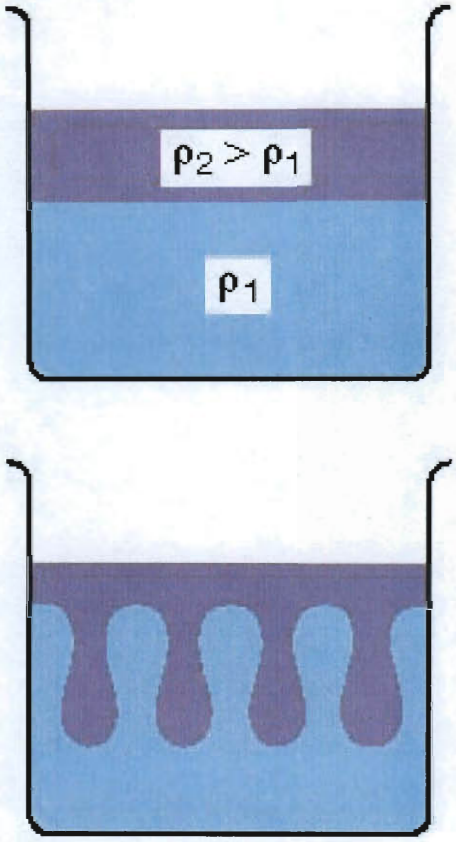

Figure 2.1. Qualitative sketch of Rayleigh-Taylor instability. Figure courtesy of T. W. Hill.

In a planetary magnetosphere, the existence of magnetized plasma adds to the complexity of the process, but a similar interchange instability can still occur if the appropriate criterion is satisfied. *Gold* [1959] first proposed the idea of interchange instability in magnetospheric physics, and stated that the interchange of different plasma populations can take place in the form of two neighboring magnetic flux tubes trading places. Figure 2.2 sketches the basic configuration of the flux-tube interchange process. Generally speaking, the centrifugal interchange instability is analogous to the Rayleigh-Taylor gravitational instability with two key modifications. Firstly, the gravitational force is replaced by the centrifugal force; secondly, the plane geometry is replaced by dipole geometry, so that the driving force is pointing radially outward instead of downward.

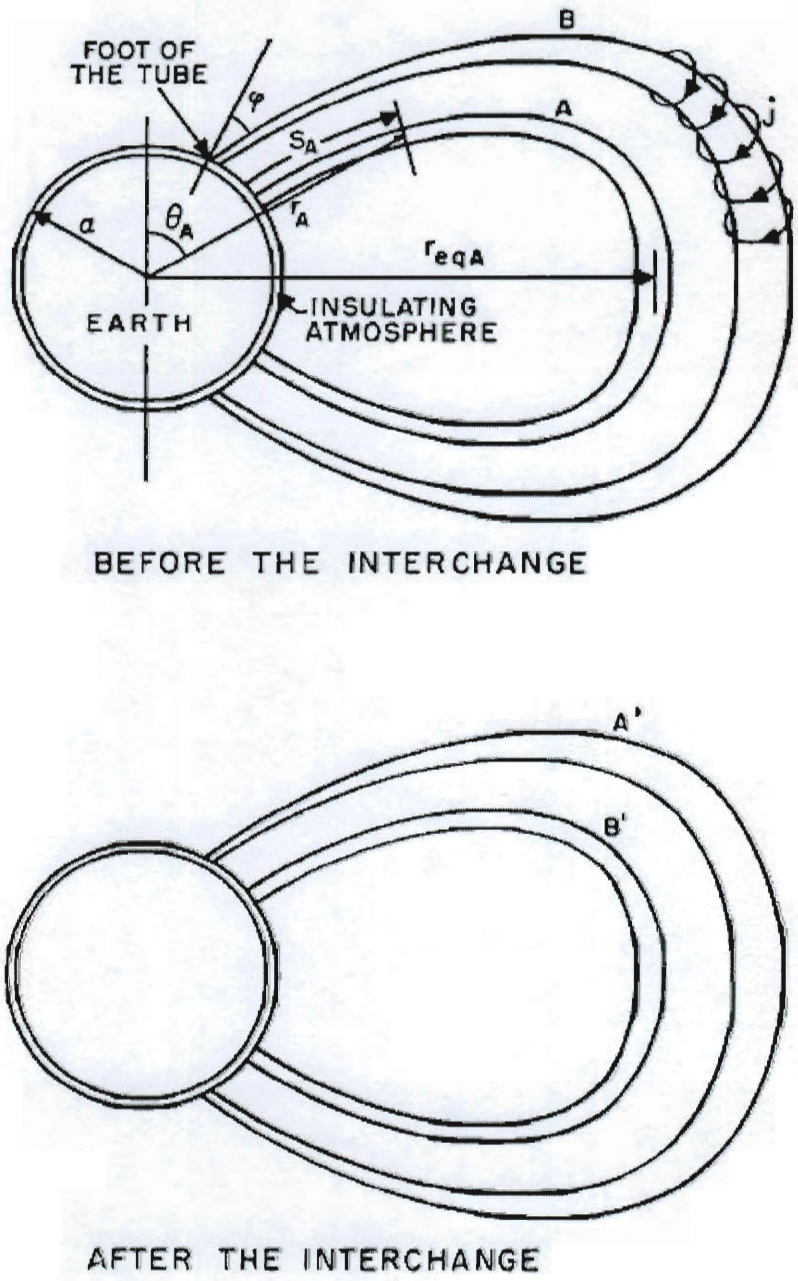

Figure 2.2. Schematic illustration of the interchange of two flux tubes with equal magnetic flux. Figure from *Sonnerup and Laird* [1963].

2.2. Interchange convection models

Many different authors (e.g., *Sonnerup and Laird* [1963]; *Xing et al.* [2007]) have studied the interchange instability and the relevant triggering criterion in Earth's magnetosphere. Rotational effects are usually negligible in Earth's magnetosphere, but become significant in the Jupiter and Saturn magnetospheres. *Melrose* [1967] first analyzed the effect of centrifugal force on the interchange instability. From a potential-energy argument, *Hill* [1976] derived mathematically the instability criterion for a rapidly rotating magnetosphere

$$\frac{\partial \eta}{\partial r_e} < 0 \qquad (2.1)$$

where η is the plasma mass content per unit magnetic flux, and r_e is the radial distance of the point where the field line crosses the equatorial plane. The inequality relation (2.1) implies that interchange motions of flux tubes driven by the centrifugal force can be triggered as long as the flux-tube mass content decreases with the equatorial crossing radial distance.

In the case of Jupiter or Saturn, the planet's rapid rotation provides the partially corotating plasma with a large centrifugal force that exceeds planetary gravity in the magnetosphere. Moreover, they both have significant internal plasma sources. For Jupiter, the mass-loading rate from Io is about 1000 kg/s [*Hill et al.*, 1983]. The corresponding value for Saturn has been estimated to be ~ 100 kg/s [e.g., *Tokar et al.*, 2006], and is one of the subjects of this thesis work described in Chapter 5 below. *Vasyliūnas* [2008] has argued that the mass input rate at Saturn by Enceladus,

although smaller in absolute units, is larger in dimensionless units (scaled to the magnetosphere's holding capacity) than that at Jupiter by Io. Therefore, the criterion of Equation (2.1) is inevitably satisfied in both Jupiter's and Saturn's magnetospheres, and theoretical models generally assume that the centrifugal interchange instability governs the plasma distribution and transport.

2.2.1. Corotating convection model

Combining the idea of *Vasyliūnas* [1978] with the mathematical formulation of *Chen* [1977], *Hill et al.* [1981] proposed a corotating convection model for Jupiter, describing a global corotating two-cell convection pattern that neglects smaller-scale longitudinal variations of plasma parameters. This model is characterized by a systematic pattern with outflow in a single "active sector" where η is above average, and inflow in the complementary sector where η is below average. Figure 2.3 illustrates the outflow sector and the associated current system. The partial ring current in the magnetosphere is connected by Birkeland (magnetic-field aligned) currents to the ionospheric Pedersen current that provides closure of the magnetospheric current. The required electric field direction corresponds to outward flow in the active sector according to the ideal MHD (frozen-in-flux) approximation $\mathbf{E} + \mathbf{v}\times\mathbf{B} = 0$.

The convection equations also lead to the important conclusion that, in the absence of plasma source or loss processes, the flux-tube mass content is conserved along streamlines, i.e., $\vec{v} \cdot \nabla \eta = 0$.

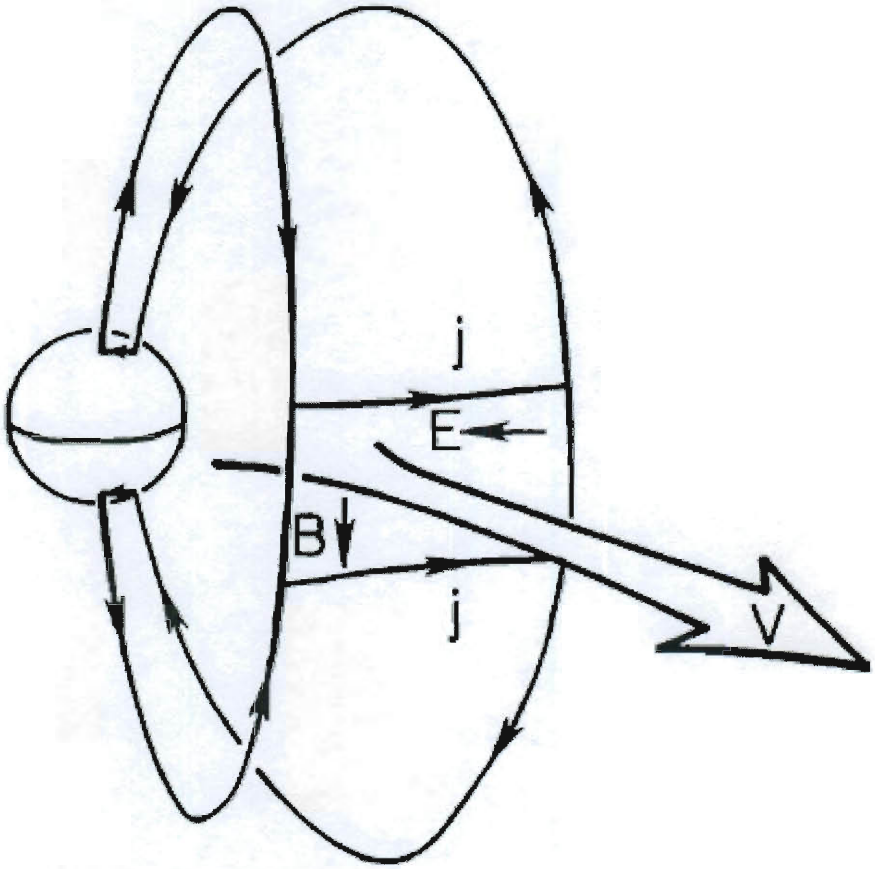

Figure 2.3. Sketch of the active outflow region in the corotating convection model, with the associated current system. Figure from *Hill et al.* [1981].

Gurnett et al. [2007] adopted the same model in order to explain observed spin periodicities in Saturn's magnetosphere, as illustrated in Figure 2.4. In the case of Jupiter, the global-scale longitudinal asymmetry that drives this global-scale convection pattern is easily attributed to the observed global-scale longitudinal asymmetry of Jupiter's intrinsic magnetic field [e.g., *Hill et al.*, 1983, and references therein]. In the case of Saturn, the observed intrinsic magnetic field is highly symmetric, and the cause of the observed magnetospheric spin periodicities remains a mystery.

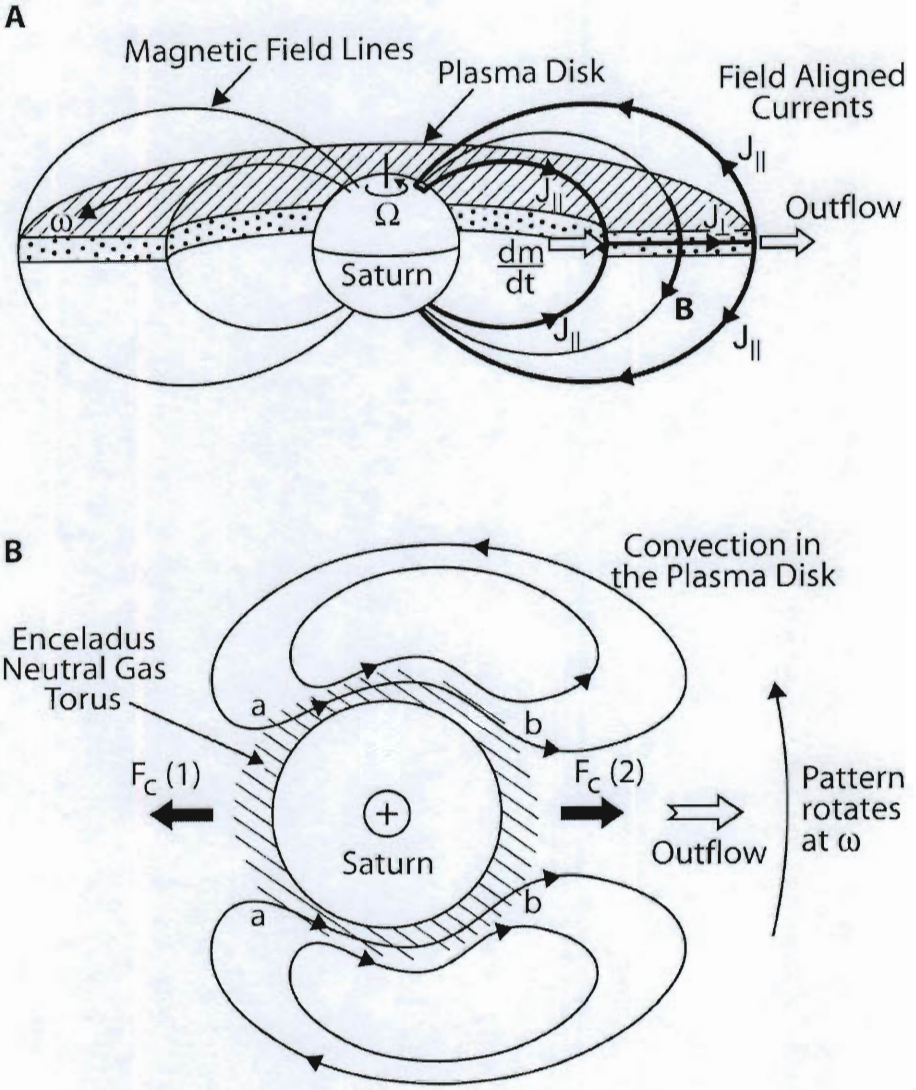

Figure 2.4. Proposed two-cell convection pattern for Saturn's magnetosphere. Upper panel (A) shows the meridional current system connecting the ionosphere and the magnetosphere (cf. Figure 1.8), with the shaded area representing the plasmasheet. Bottom panel (B) shows the proposed corotating two-cell convection pattern, which could generate the observed rotational modulation of magnetospheric effects. Figure from *Gurnett et al.* [2007].

2.2.2. Transient flux tube model

Pontius et al. [1986] proposed an alternate model to describe steady state transport in Jupiter's centrifugally unstable plasma distribution. They considered the steady motions of small discrete flux tubes, whose plasma content is significantly different from the longitudinally averaged value. They adapted the convection equations of *Hill et al.* [1981] for the small-scale motions of these isolated flux tubes of unspecified sizes, and included micro-diffusion effects in the interchange process. In their model, plasma transport takes place through these small-scale motions, while each flux tube conserves its plasma mass content η over large distances. Figure 2.5 illustrates the isolated flux tubes and associated currents, where isolated transient flux tubes move inward or outward through a uniform background. According to this model, denser transient flux tubes containing dense plasma tend to move outward, while more tenuous ones with hotter more tenuous plasma move inward. This can be viewed as one of the theoretical bases of our observational study.

Pontius and Hill [1989] further presented analytical calculations assuming isolated convection structures with elliptical shape. They gave equations to describe the motion of a transient flux tube that differs in plasma content from the background by an amount $\Delta\eta$, and showed that a mass-loaded isolated flux tube accelerates radially outward at the rate $v_r \propto r^4$.

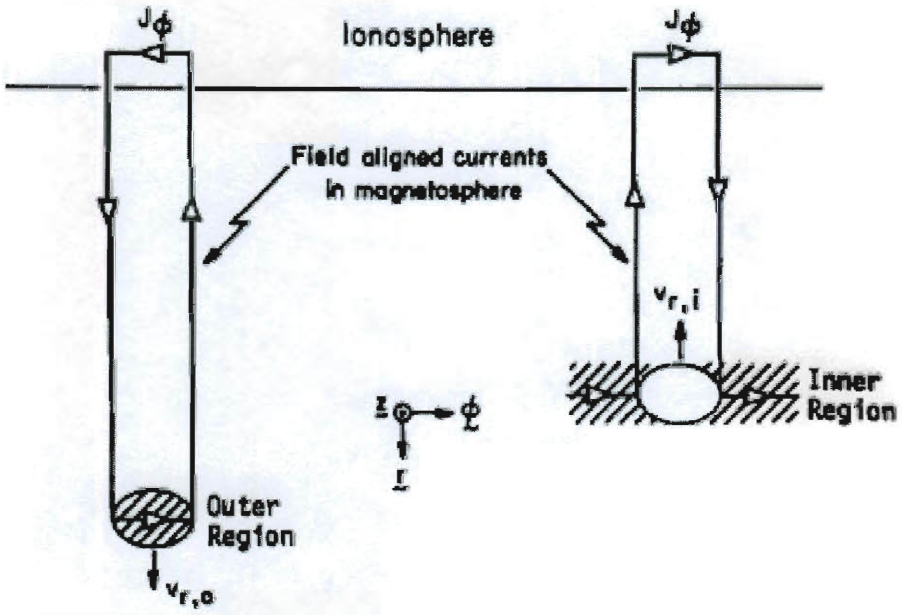

Figure 2.5. Schematic illustration of isolated flux tubes and associated currents (from *Pontius et al.* [1986]).

2.2.3. Radial diffusion model

Early theoretical efforts include models that are based on the radial diffusion process [e.g., *Siscoe and Summers,* 1981; *Vasyliūnas*, 1989], which focus on random small-scale circulatory motions and assume that bulk plasma transport takes place stochastically through the random interchange motions of many small turbulent circulation cells (Figure 2.6), instead of alternating channels of systematically outward and systematically inward flow. This approach neglects longitudinal variations, and applies longitudinally averaged values to any parameters related to the small-scale motions. Radial diffusion models have the advantage of being analytically tractable in one dimension (the radial dimension), but have conceptual difficulties in their basic assumptions and their applicability is questionable [*Hill* et al., 1983; *Pontius et al.,* 1986].

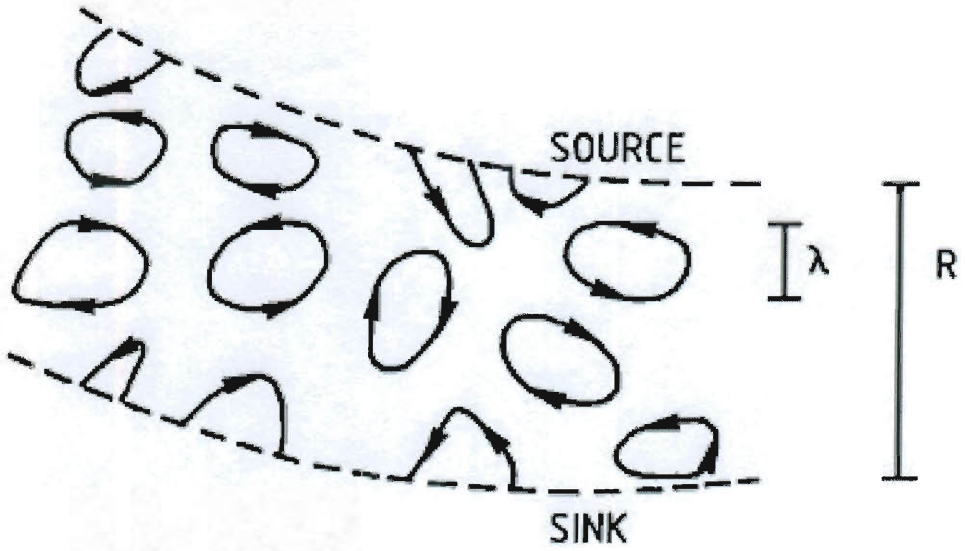

Figure 2.6. Sketch of instantaneous flow line configuration in the radial diffusion model (from *Vasyliūnas* [1989]).

2.3. Observational background

Observations at both Jupiter and Saturn, especially the latter, have provided overwhelming evidence in favor of models based on the centrifugal interchange instability. Since the beginning of its orbital mission, the Cassini spacecraft has provided direct observational evidence for rotationally driven plasma radial transport in Saturn's magnetosphere [*André et al.*, 2005; *Burch et al.,* 2005; *Hill et al.,* 2005; *Mauk et al.,* 2005]. Meanwhile, numerical simulations have suggested a picture of centrifugally driven radial transport that includes alternating longitudinal sectors, or "fingers", of outflow and inflow [*Yang et al.,* 1994; *Liu and Hill*, 2009]. It is feasible now to do definitive observational tests of both the previous theories and the recent numerical simulations, using the observations provided by Cassini.

Although the idea of centrifugally driven plasma transport at Jupiter and Saturn has been widely accepted for many years, there have been few opportunities for observational study of the size and shape of the resulting convection cells until the beginning of the Cassini era. This thesis is devoted to revealing the details of the centrifugally driven radial plasma transport process in Saturn's inner magnetosphere through analysis of data measured by the CAPS instrument.

3. The Cassini Plasma Spectrometer

The following description is extracted from *Young et al.* [2004]. The Cassini Plasma Spectrometer (CAPS) is one of the twelve instruments onboard the Cassini spacecraft, which was launched in October 1997 and entered into orbit around Saturn in July 2004. CAPS consists of three sensors, the Electron Spectrometer (ELS), the Ion Mass Spectrometer (IMS) and the Ion Beam Spectrometer (IBS). The basic design goal of CAPS is to obtain comprehensive three-dimensional measurements of the various plasma populations including the composition of all major atomic and molecular ions from 1 to 50,000 eV. Figure 3.1 shows the optical layout and basic structure of CAPS in the azimuthal (X-Y) plane of the Cassini spacecraft.

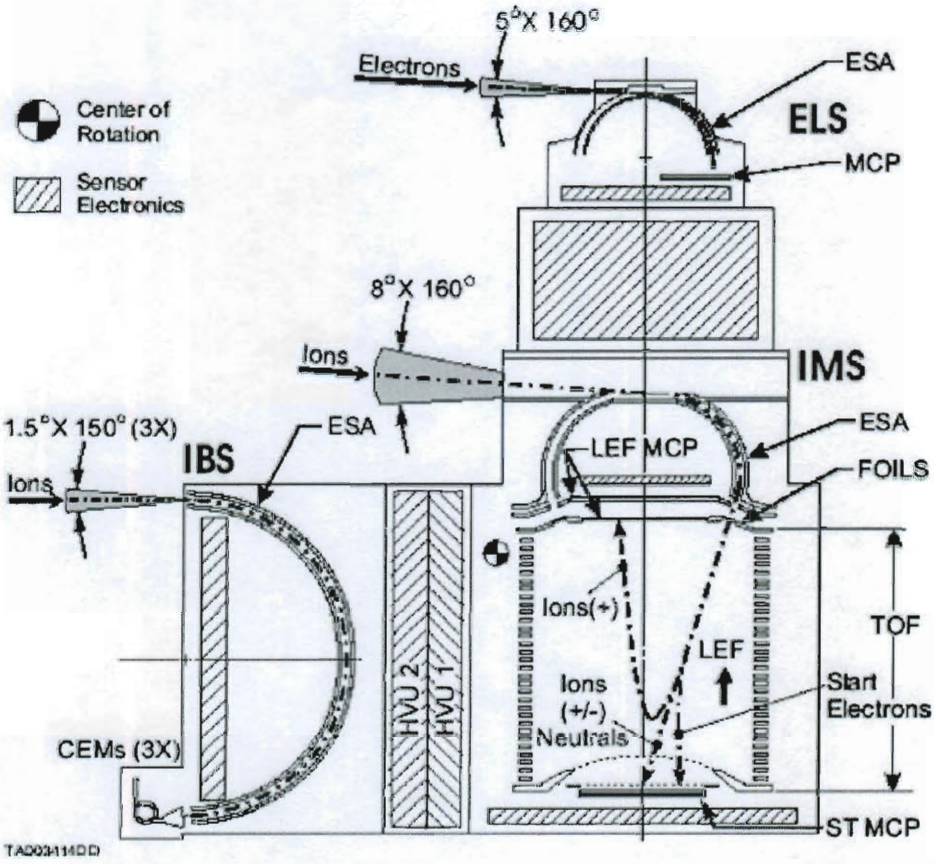

Figure 3.1. Optical layout and key elements of CAPS. Dash-dotted lines represent typical particle trajectories. This figure is from *Young et al.* [2004].

The ELS contiguously measures velocity distributions of electrons with energies ranging from 0.6 eV to 28,250 eV in 63 energy bins. It is a hemispherical top-hat electrostatic analyzer (ESA). Electrons enter a baffled collimator structure and undergo electrostatic analysis between two concentric spherical plates. The outer plate is grounded with zero voltage, and the inner plate takes a series of positive high voltages corresponding to the 63 energy bins, and the voltage is swept every two seconds. The energy resolution ($\Delta E/E$) is approximately 17%. There are eight anodes, each of which has an angular coverage of $20° \times 5°$.

The IMS is a high-sensitivity, high-resolution ion mass spectrometer, which is designed to measure composition of hot, diffuse magnetospheric ions between 1 eV and 50,280 eV, also with a resolution of $\Delta E/E = 17\%$. The IMS covers this energy range contiguously, also in 63 energy bins, and spends 4 seconds sweeping through all the energy steps. It simultaneously measures ion mass per charge (M/Q) from 1 to 100 atomic mass units (amu) per electron charge, with a mass resolution of $M/\Delta M \approx 60$. Similar to the ELS, the IMS also has eight anodes aligned in the elevation plane, providing an instantaneous angular coverage of $\sim 160° \times 8°$.

The third sensor, the IBS, measures ion beams with very high energy resolution ($\Delta E/E = 0.014$) from 1 eV to 49,800 eV. It has three anodes that are tilted and offset from one another in the vertical direction, so that the IBS covers approximately $1.4° \times 150°$ instantaneous field-of-view (FOV).

Table 3.1 shows the relevant parameters with regard to the performance of all the CAPS sensors. All three sensors of CAPS have in common that they detect electrons and ions based on the charged particle motions in electrostatic fields. The ELS and IBS separate electrons and ions by energy/charge ratio (E/Q) and by elevation angle of arrival. Only particles within a particular range of E/Q and direction of arrival can pass the ESA. The IMS also takes advantage of these quantities to separate ions, but in addition disperses them by a time-of-flight (TOF) mass spectrometer.

Parameter	IMS		ELS	IBS
	Med. Res.	High Res.		
Energy/charge response				
Range (eV/e)	1–50,280		0.6–28,750	1–49,800
Resolution $(\Delta E/E)_{FWHM}$	0.17		0.17	0.014
Angular response				
Elevation sectors (number)	8		8	3
Instantaneous FOV $(AZ \times EL)_{FWHM}$	$8.3° \times 160°$		$5.2° \times 160°$	$1.4° \times 150°$
Angular resolution $(AZ \times EL)_{FWHM}$	$8.3° \times 20°$		$5.2° \times 20°$	$1.4° \times 1.5°$
Mass/charge response				
Range (amu/e)	$1 \sim 400$	$1 \sim 100$	–	–
Resolution $(M/\Delta M)_{FWHM}$	8	60	–	–
Energy-geometric factor*				
(cm^2 sr eV/eV)	5×10^{-3}	5×10^{-4}	1.4×10^{-2}	4.7×10^{-5}
Temporal response				
Per sample (s)	6.25×10^{-2}		3.125×10^{-2}	7.813×10^{-3}
Energy-elevation (s)	4.0		2.0	2.0
Energy-elevation-azimuth (s)			180	

*Applies to total field-of-view and includes efficiency factors.

Table 3.1 Summary of CAPS sensor performance parameters (from *Young et al.* [2004]).

Because the CAPS instrument is fixed with the body of the non-spinning Cassini spacecraft, its field-of-view is constrained by the spacecraft orientation. A motor actuator is designed as an effort to overcome this limitation (Figure 3.2). Mounted on this rotating platform, CAPS is able to rotate by ~ 180° along the direction of the spacecraft Z-axis, thus obtaining maximum field-of-view in the azimuthal direction. Figure 3.2 also shows the location and orientation of CAPS on the Field and Particles Pallet of the spacecraft.

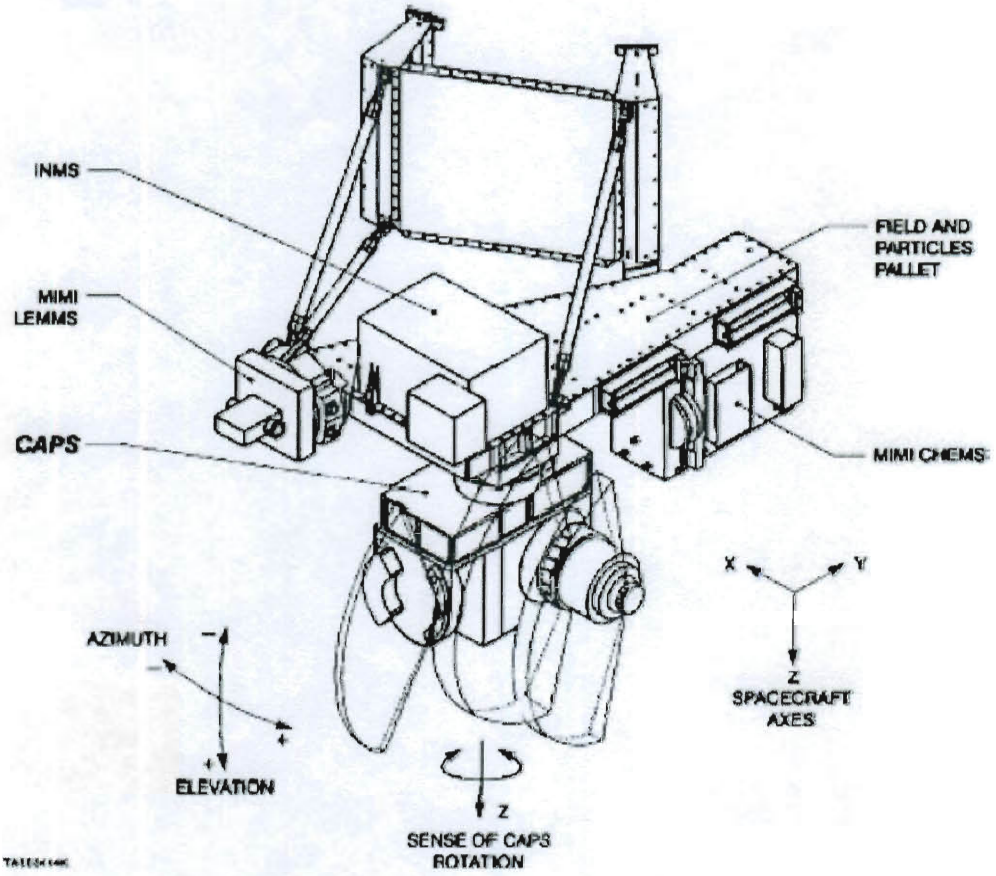

Figure 3.2. Sketch of CAPS and its neighboring instruments onboard the Cassini spacecraft. CAPS is shown mounted on a rotating platform. The figure also shows the spacecraft coordinate system [*Young et al.*, 2004].

With the actuating platform, approximately 56% of the full 4π steradian sky can be swept about every three minutes. Figure 3.3 shows the all-sky projection of the CAPS field-of-view (FOV). Note that surrounding structures onboard the spacecraft (e.g., the LEMMS instrument) also restrict the FOV.

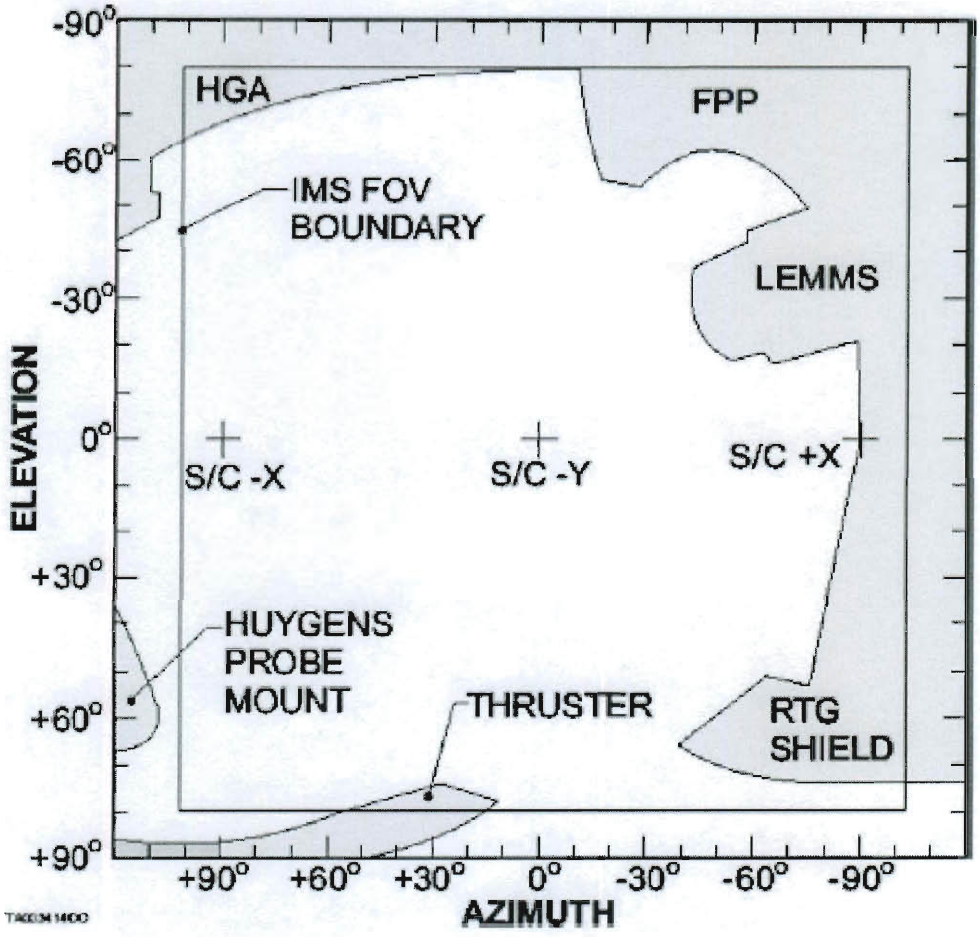

Figure 3.3. All-sky projection of the CAPS IMS field-of-view (FOV). A similar FOV also applies to ELS and IBS. Shaded areas represent the encroachment on the field of view caused by surrounding structures [*Young et al.*, 2004].

4. Statistical analysis of injection/dispersion events in Saturn's inner magnetosphere

In the inner magnetosphere of a rapidly rotating planet such as Jupiter and Saturn, radial transport of plasma mainly comprises hot, tenuous plasma moving inward and cold, denser plasma moving outward. A distinctive phenomenon resulting from the drift dispersion of injecting hot plasma provides direct evidence for this convective motion. Particle instruments aboard the Cassini spacecraft, including the Magnetospheric Imaging Instrument (MIMI) and the Cassini Plasma Spectrometer (CAPS), have made numerous observations of such signatures. In this chapter, the statistics of the properties of such events are studied by analyzing CAPS data from 26 Cassini orbits.

4.1. Introduction

As we have discussed in Chapter 2, in a rotation-dominated magnetosphere with internal plasma sources, radial transport of plasma is expected to be triggered by the centrifugal interchange instability [*Hill*, 1976], in which cold flux tubes with larger densities move outward and exchange locations with hotter, more tenuous flux tubes. The process of this radial convection with alternative inflow and outflow sectors has been studied by numerous theoretical models [e.g., *Hill et al.*, 1981; *Pontius et al.*, 1986] and numerical simulations [*Yang et al.*, 1994; *Wu et al.*, 2007a, b], and was confirmed by observations in Jupiter's magnetosphere [*Mauk et al.*, 1997, 1999].

While moving in the radial direction, electrons and ions with different energies become dispersed in the longitudinal direction and hence arrive at the spacecraft at different times. Observational signatures of this process on the energy-time spectrograms are referred to as injection/dispersion events, and have been observed frequently by the Cassini Plasma Spectrometer (CAPS) [*Young et al.*, 2005] and the Cassini Magnetospheric Imaging Instrument (MIMI) [*Krimigis et al.*, 2005] since Cassini's first orbit at Saturn in July, 2004. Figure 4.1 shows the typical appearance of injection/dispersion signatures in the log-scale energy versus time spectrograms for both electrons and ions, observed by Electron Spectrometer (ELS) and Ion Mass Spectrometer (IMS), respectively. Similar signatures have been observed by the MIMI instrument for higher-energy electrons and ions. Several previous studies [e.g., *Burch et al.*, 2005; *Hill et al.*, 2005; *Mauk et al.*, 2005] have interpreted these events as evidence for interchange instability in Saturn's magnetosphere.

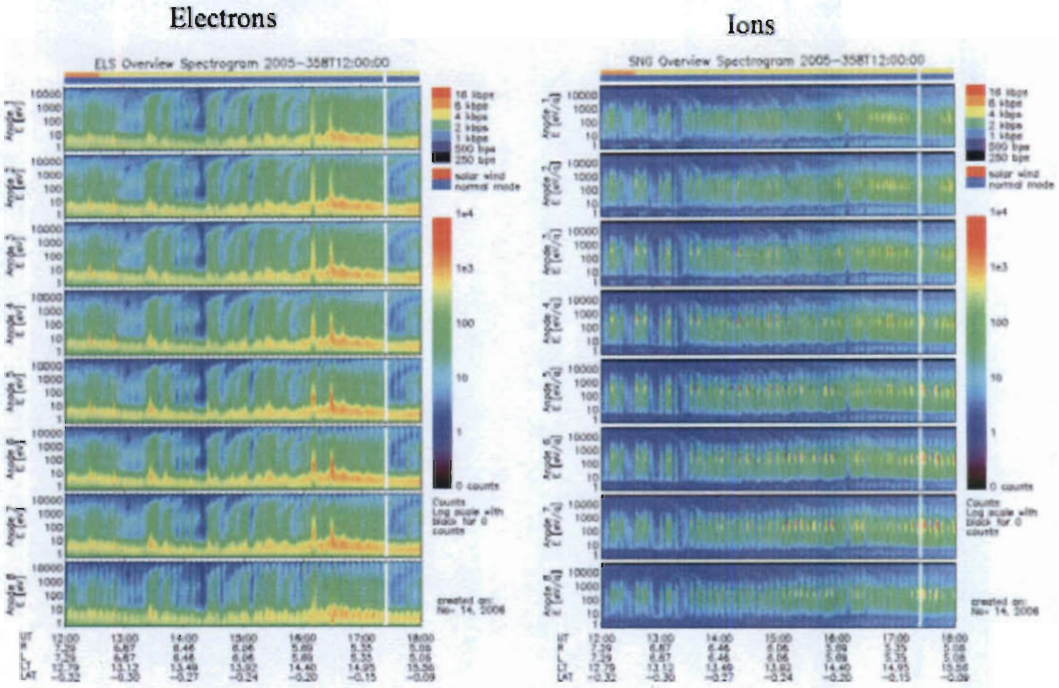

Figure 4.1. Injection/dispersion signatures in sample log-scale energy versus time spectrograms for electrons (left) and positive ions (right) observed by CAPS. Both spectrograms contain 6-hour data of counts recorded by the eight anodes of ELS and IMS.

Figure 4.2, reproduced from [*Hill et al.*, 2005], shows a localized injection of hot plasma accompanied by adiabatic gradient and curvature drifts. It is expected that while particles are injected by **E×B** drift in the radial direction, gradient-curvature drifts in the longitudinal direction will separate electrons from ions, forming a V-shaped structure in a linear energy versus longitude spectrogram. Therefore, this picture is considered as the physical mechanism to trigger the injection/dispersion events. In addition, *Hill et al.* [2005] pointed out that these events are more prominent in observations at Saturn than at Jupiter because the gradient-curvature drift speed is about 25 times faster at Saturn for a given energy at a given dipole L value.

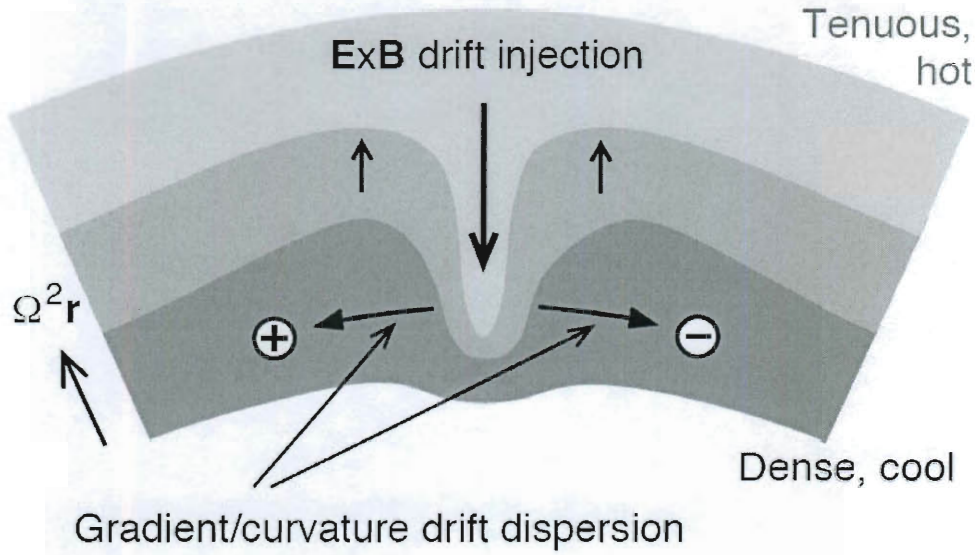

Figure 4.2. Conceptual illustration of an injection-dispersion event, reproduced from Figure 1 of *Hill et al* [2005].

Because these structures are swept past the spacecraft by the fast rotational flow, they can be directly observed on a linear energy versus time spectrogram (Figure 4.3, reproduced from *Hill et al.*, 2005). Straight lines were fit to each leg of the "V" in order to analyze the properties of each event, with ions forming the left halves and electrons forming the right halves. In Saturn's corotating frame, gradient and curvature drifts move electrons westward and ions eastward. Therefore, in an energy-time spectrogram, high-energy ions are expected to be observed first, followed in sequence by lower-energy ions, lower-energy electrons and finally high-energy electrons.

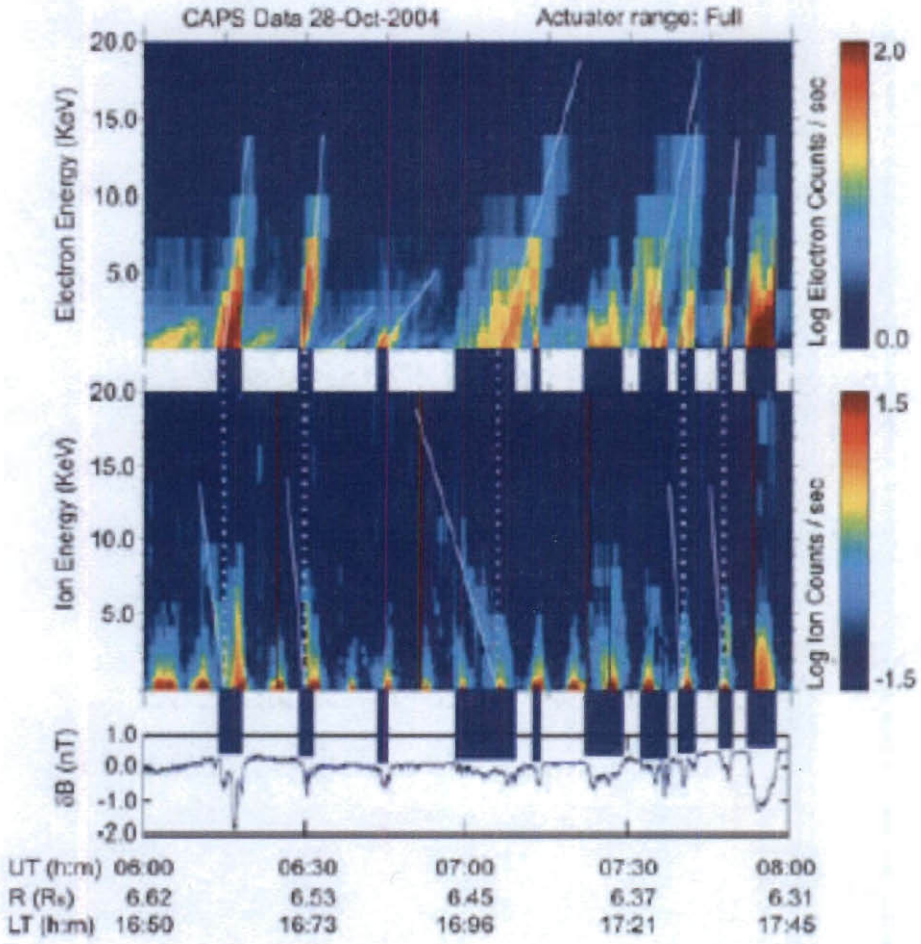

Figure 4.3. Examples of injection/dispersion signatures in linear energy-time spectrograms observed by CAPS instrument, reproduced from Figure 2 of *Hill et al.* [2005]. Top and middle panels are for electrons and position ions, respectively. The bottom panel shows simultaneous magnetic field perturbations observed by the Cassini MAG experiment, after subtracting a cubic fit to the large-scale variation.

4.2. Geometric properties of injection/dispersion events

As the injection/dispersion process develops with time, the distance between ions and electrons grows. The age of the injection is inversely proportional to the slope of each leg of the V structure. For standard gradient/curvature drifts in Saturn's dipole magnetic field, the relationship is

$$\frac{dE}{dt} = \left(-6.87\frac{keV}{\min}\right)\left(\frac{10}{L}\right)\left(\frac{1hr}{T_{inj}}\right)\left(\frac{\Omega}{\Omega_S}\right) sign(q). \tag{4.1}$$

Here L denotes the dipole L value (equatorial distance in units of Saturn's radius R_S = 60,268 km), Ω_S represents Saturn's rotation frequency, Ω is the angular velocity at which an injection/dispersion structure is swept past the spacecraft by the rotational flow, T_{inj} is the time since injection, and q is the particle charge. Strictly speaking, this equation assumes the injection/dispersion process takes place in the equatorial plane. Our study only covers a very limited latitude range, so it is adequate to use this equation. Moreover, Equation (4.1) strictly applies only for particles mirroring in the equatorial plane, but it is adequate for particles of any pitch angle within a factor of order unity.

Other properties of these events can also be estimated from observation. For example, the longitudinal width can be obtained by multiplying the width in time Δt by the partial corotation velocity, i.e.,

$$W = L R_S \Omega \Delta t . \tag{4.2}$$

The local time of injection is related to the local time of observation by

$$LT_{inj} = LT_{obs} - \Omega T_{inj} . \tag{4.3}$$

Finally, the injection longitude can be calculated from

$$\lambda_{inj} = \lambda_{obs} - \left(\Omega_S - \Omega\right) T_{inj} . \tag{4.4}$$

Hill et al. [2005] reported about 100 such events observed by CAPS during Cassini's first two orbits of Saturn, with a subset of 48 selected for study. Their work included a statistical analysis, which indicated that the ages of the injection/dispersion events ranged from several hours to several Saturn rotation periods, and longitudinal widths ranged from less than one Saturn radius to several radii. In addition, most of the events were located in the radial range $5 \leq L \leq 10$, while the local time distribution and longitude distribution were both random in appearance. The assumption of rigid corotation was made ($\Omega = \Omega_S$) because at that time there was not enough analysis of the ion velocity moments to provide azimuthal velocities. This assumption was an overestimate of rotational velocity; as a result, ages, widths and injection longitudes were overestimated, while injection local times were underestimated.

4.3. Analysis of properties

We continue the statistical analysis of the properties of the injection/dispersion events, and extend it to a larger sample space. With many more orbits of observation since Cassini's Saturn Orbit Insertion (SOI), we are now able to include a much larger data set in our study, extending from June 2004 to the end of August 2006. Similar methods to those of *Hill et al.* [2005] are used to estimate the characteristics of the injection/dispersion structures.

Rotational velocities in the azimuthal direction can be overestimated by simply assuming rigid corotation. Therefore, in addition to expanding the statistical data set, we try to improve the statistical results by utilizing observed rotational velocities that were reported recently by *Wilson et al.* [2007] (Figure 4.4). The following second-order polynomial fit to the measurements of *Wilson et al.* is used to specify $\Omega(L)$ in equations (4.1), (4.2), (4.3) and (4.4).

$$V_\varphi = 79.56 - 13.06R + 1.30R^2. \tag{4.5}$$

Here V_φ is the rotational velocity in km/s and R is the radial distance in R_S. This is an improvement over the rigid corotation assumption, although we still have to assume that the azimuthal velocity is the same at all longitudes on a given L-shell.

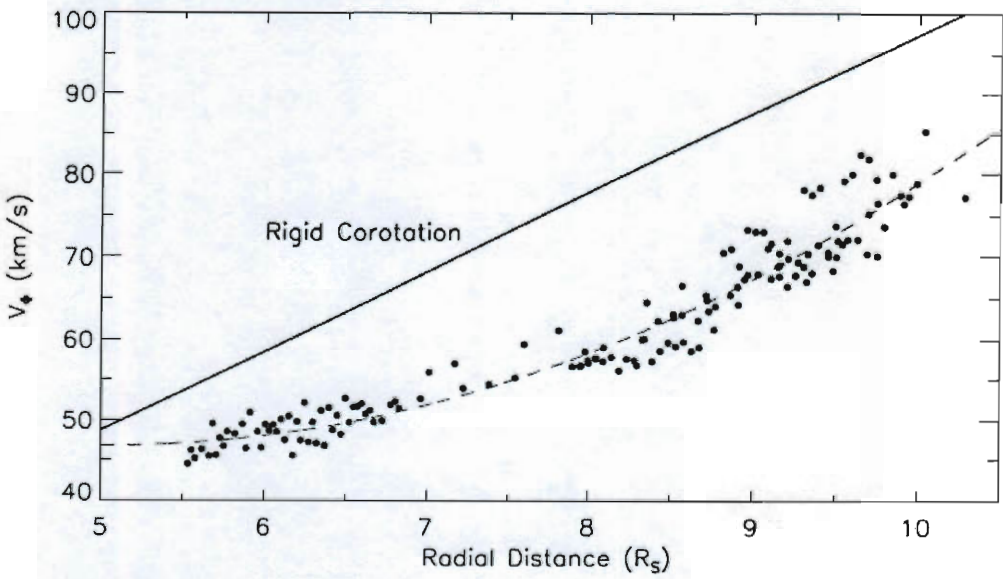

Figure 4.4. Rotational flow velocities measured by CAPS/IMS, adapted from *Wilson et al.*, 2007. The straight line represents rigid corotation, while the dotted points represent measured data of partial corotation velocities. The dashed curve represents the fourth-order polynomial fit (Equation (4.5)) to these data points.

As before, the analysis procedure still depends on subjective judgment, which inevitably introduces errors when reading the observable properties from the spectrograms. To limit the impacts of this error source, we adopt a set of selection criteria to limit our analysis to the most unambiguous events. Specifically, each event we selected here has an identifiable center time, i.e., the intersection of the structure legs with the time axis; the width of the legs must also be identifiable; and the slopes of the legs must be reliably measurable. With these criteria, we selected 429 structures for analysis, located between the radial distances 4.6 and 14.8 Saturn radii. Of these 429 events, 410 clustered between L values of 5 and 10, i.e., more than 95% of the total.

The results reported below are based on the CAPS Electron Spectrometer (ELS) electron data only. Many of the structures do not have clear ion components, because ion count rates are much lower than electron count rates in a given plasma environment.

4.4. Statistical results

Here we use histograms to display statistical distributions of various properties of injection/dispersion events. In Figure 4.5, the upper panel shows the age distribution of all 429 events, while the bottom panel shows the distribution of longitudinal widths. One can conclude that most of the events have ages of less than two hours and widths of less than one Saturn radius. However, some events are as old as several

Saturn rotation periods, and as wide as several Saturn radii. These results are consistent with those of *Hill et al.* [2005]. Note that the lower limits on both the ages and the widths are among the selection criteria, so that very young events, as discussed by *Burch et al.* [2005], might not be identified here. The lower limit for ages is about 0.25 hours, while the lower limit for widths is about 0.1 R_S. Upper limits on ages and widths are also implied by the selection criteria, which tend to rule out both very old structures and very large-scale ones.

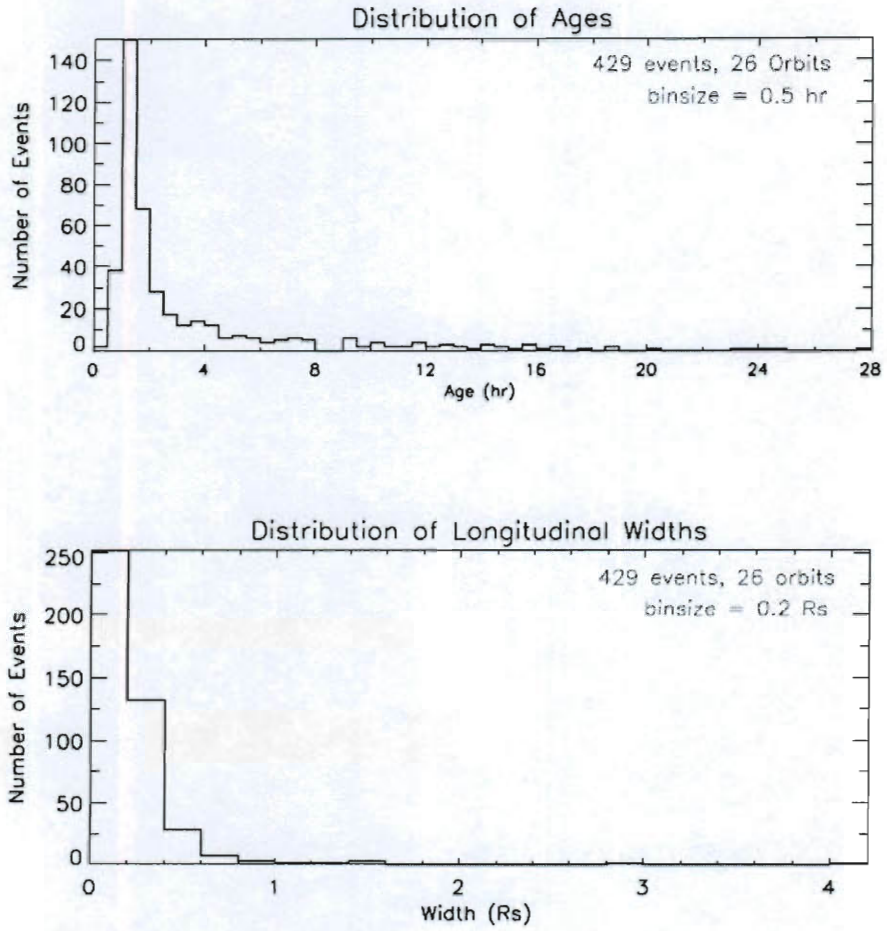

Figure 4.5. Statistical distributions of the ages (top panel) and the longitudinal widths (bottom panel) of 429 injection-dispersion events selected from 26 orbits of Cassini Plasma Spectrometer data (from *Chen and Hill*, [2008]).

One thing that we are interested in is the distribution of injection longitudes, from which we can obtain information about the modulation of these events by Saturn's rotating magnetosphere. A recently defined longitude system, the Saturn Kilometric Radiation (SKR) system [*Kurth et al.*, 2007], is now widely used, and is also known as the SLS2 system [*Kurth et al.,* 2008]. It is a dynamic system with a variable period that follows the rotational modulation. Several magnetospheric phenomena have been reported to be well organized by this system, including SKR itself by definition [*Kurth et al.*, 2007], magnetic field perturbations [*Giamperi et al.*, 2006], electron density in the inner magnetosphere [*Gurnett et al.,* 2007], and the energetic particle flux in the outer magnetosphere [*Carbary et al.*, 2007a]. An immediate question hence arises: could the injection/dispersion events also be modulated by this SKR longitude system? Our analysis is motivated in part to address this question, using data obtained in the time range from January 2004 to August 2006, when the SKR system was accurately applicable [*Kurth et al.*, 2008].

In Figure 4.6, the upper panel shows the distribution of occurrence frequencies of the injection/dispersion events versus their injection longitude in the SKR system. To obtain the occurrence frequency in a given longitude bin, we divide the number of events found in that bin by the time Cassini spent in the same sector. From the histogram, we conclude that the occurrence of injection/dispersion events is randomly distributed with regard to injection longitude in the SKR system, as there is no obvious clustering at any particular longitude.

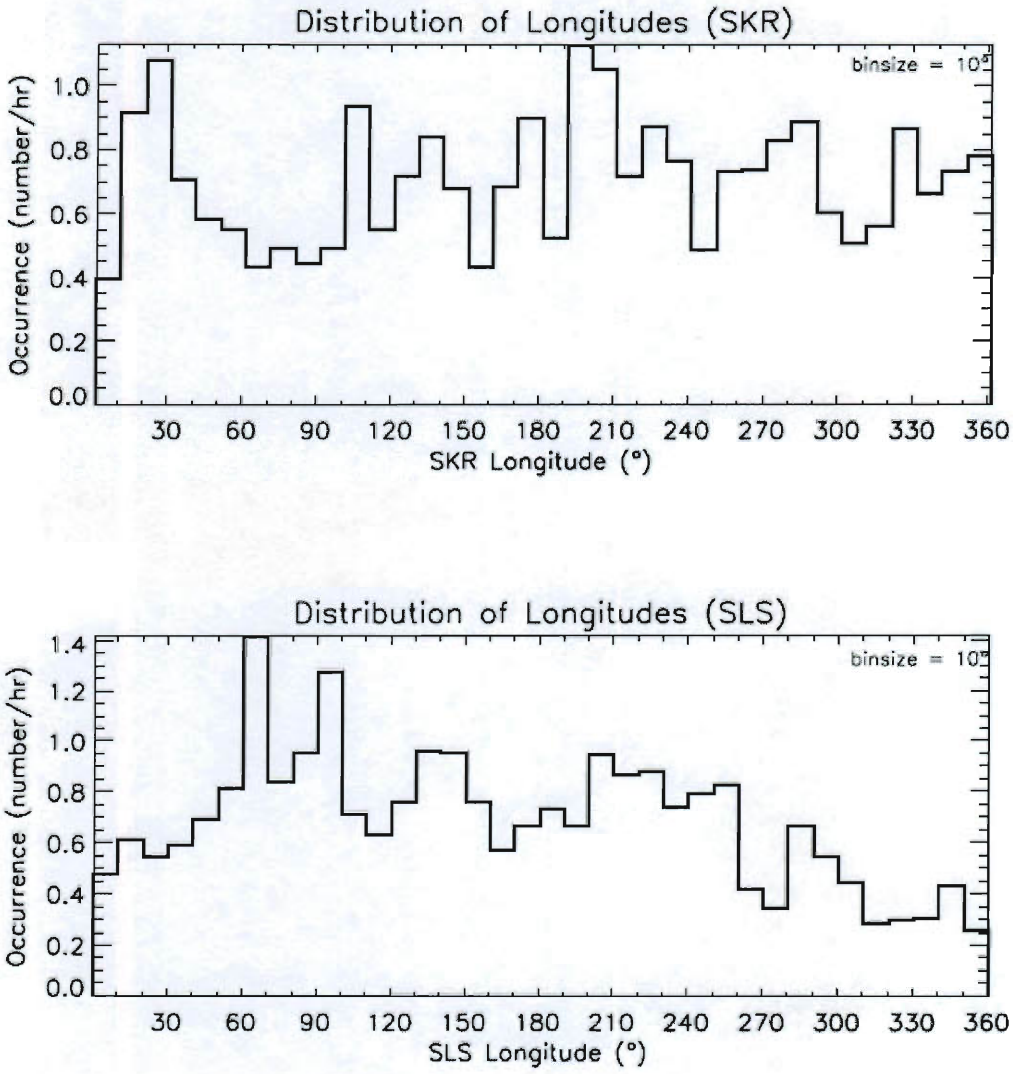

Figure 4.6. Statistical distributions of the injection longitudes for two different systems, SKR (top) and SLS (bottom) (from *Chen and Hill*, [2008]). Only those 410 events located inside the radial distance range [5,10] are included. Here the vertical axes represent the occurrence frequencies instead of number of events.

Interestingly, a different picture (bottom panel, Figure 4.6) emerges when we use the SLS (Saturn Longitude System) [*Seidelmann et al.*, 2002] instead of the SKR system. SLS was adopted by the International Astronomical Union (IAU) based on Voyager-era observations of the period of SKR. The injection/dispersion events seem to be organized surprisingly well by SLS longitude, in that the occurrence frequency is systematically larger in the longitude range ~ 50° - 250° than outside this range.

The SLS longitude modulation is surprising when we consider that most other magnetospheric phenomena have been found to be modulated by the SKR system. Could this modulation in the SLS system be a sporadic or transient effect? A persistence test is designed to check the persistence of the data in time. We simply separate the data set into two halves by time, and plot the histogram of occurrence frequencies for each half. The results are shown in Figure 4.7, where the first half of the data is plotted in the upper panel and the second half in the bottom one. There is an apparent modulation in both halves, but also a "phase shift" between the first half and the second half. This phase shift suggests that the modulation period, if any, is not SLS exactly, but slower by about one part in 2000. (By comparison, the SKR rate is about 1% slower than the SLS rate.)

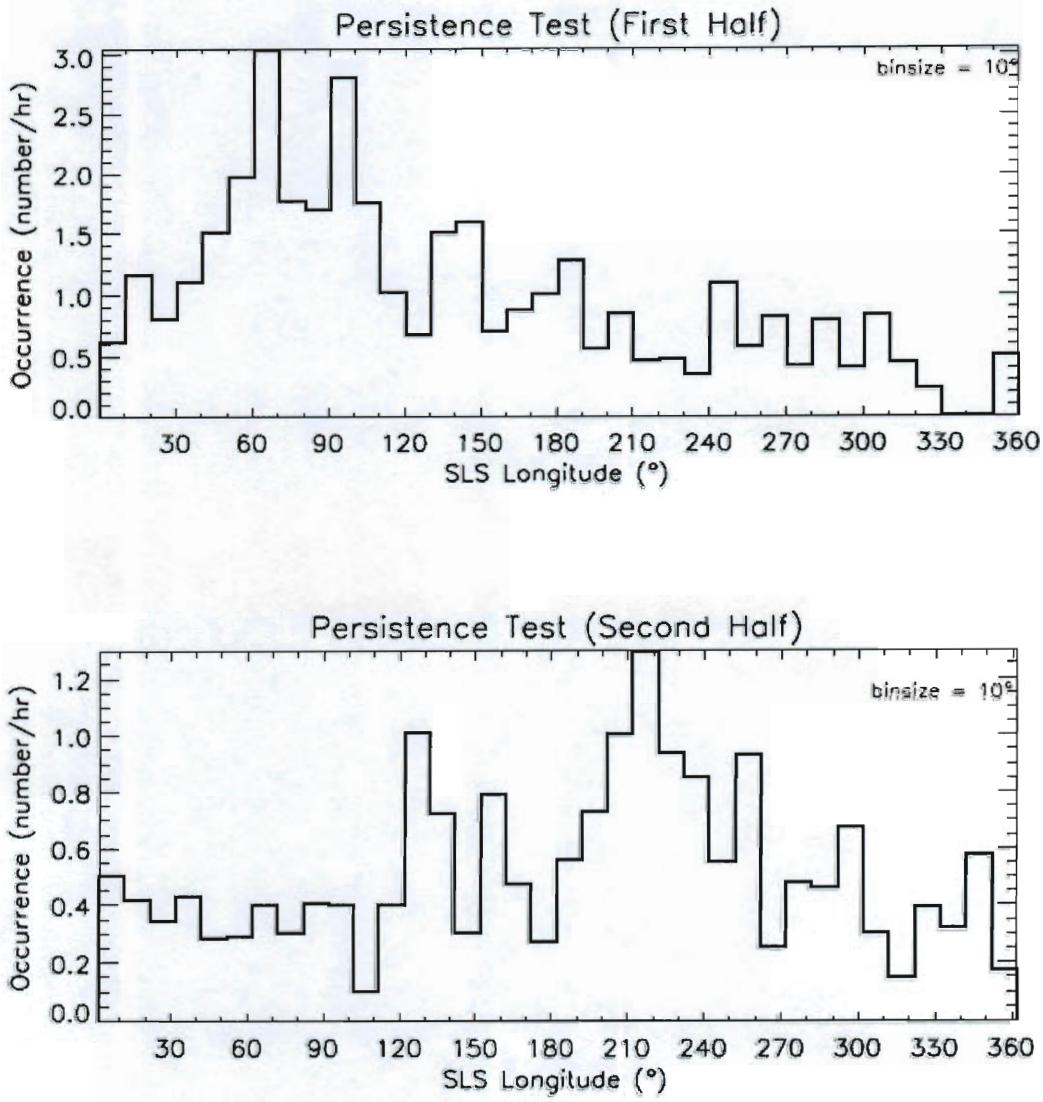

Figure 4.7. Persistence test of the longitudinal modulation in the SLS system (from *Chen and Hill*, [2008]). The upper and lower plots display the distributions of the injection longitudes (SLS) for the first and second halves by time, respectively. Only the 410 events located inside the radial distance range [5,10] are included.

In addition to the rotational modulation of magnetospheric phenomena, a spiral pattern has been identified by *Espinosa et al.* [2003], *Cowley et al.* [2006], and *Gurnett et al.* [2007] in magnetic field perturbations, and by *Carbary et al.* [2007b] in high-energy electron fluxes (28 keV – 48 keV) in the SKR longitude system, at radial distances larger than 10 Saturn radii. To investigate whether there is a similar modulation pattern in the injection/dispersion events, we plot these events in the equatorial plane of the polar SKR coordinate system (Figure 4.8), showing both their radial and longitudinal locations. Note that the longitude coordinate is a left-handed angle. No spiral pattern is apparent, although we cannot rule out the possibility of multiple short-lived spirals having different phases.

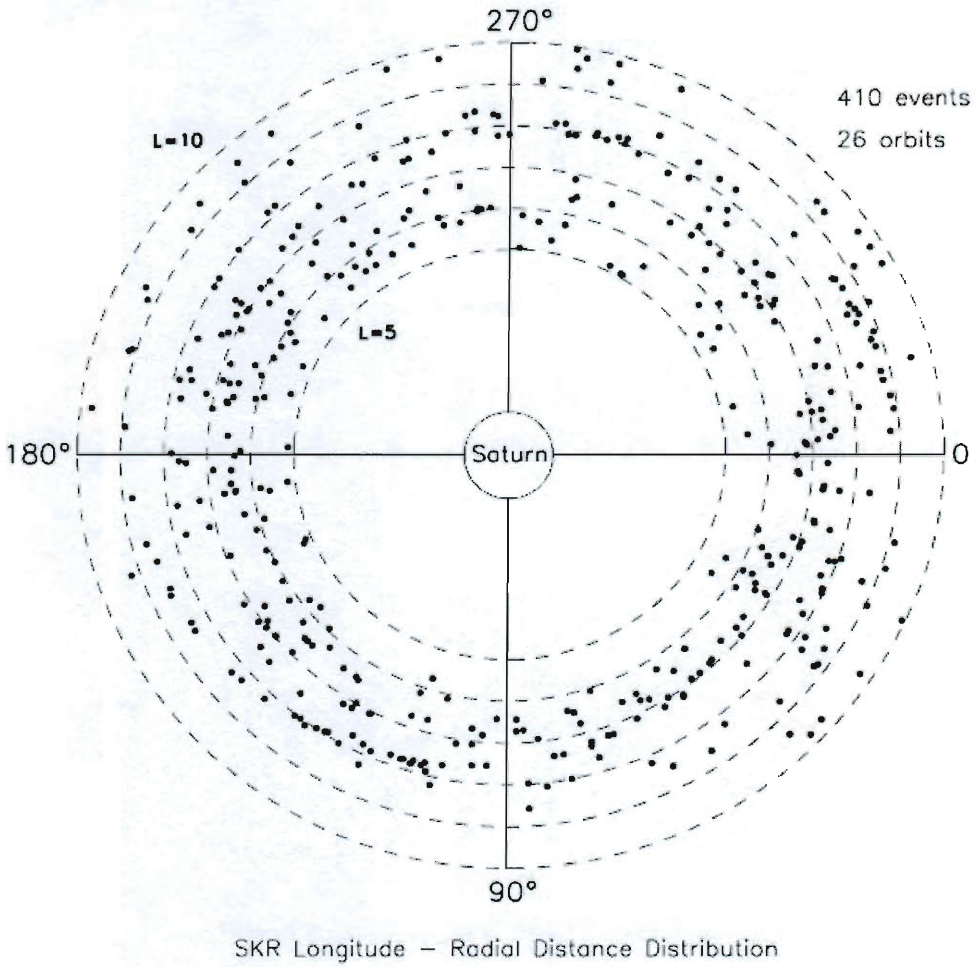

Figure 4.8. Statistical distributions of the injection longitudes (SKR) in the polar coordinate system (from *Chen and Hill*, [2008]). Only the 410 events located inside the radial distance range [5,10] are included.

To show the local-time distribution of injections, we plotted a histogram of occurrence frequency versus different local time bins (Figure 4.9). There is an apparent local-time asymmetry, with a clustering of plasma injections in the pre-noon quadrant. This is certainly not the local-time distribution that one would expect from an Earth-like convection system in which virtually all injections occur on the night side.

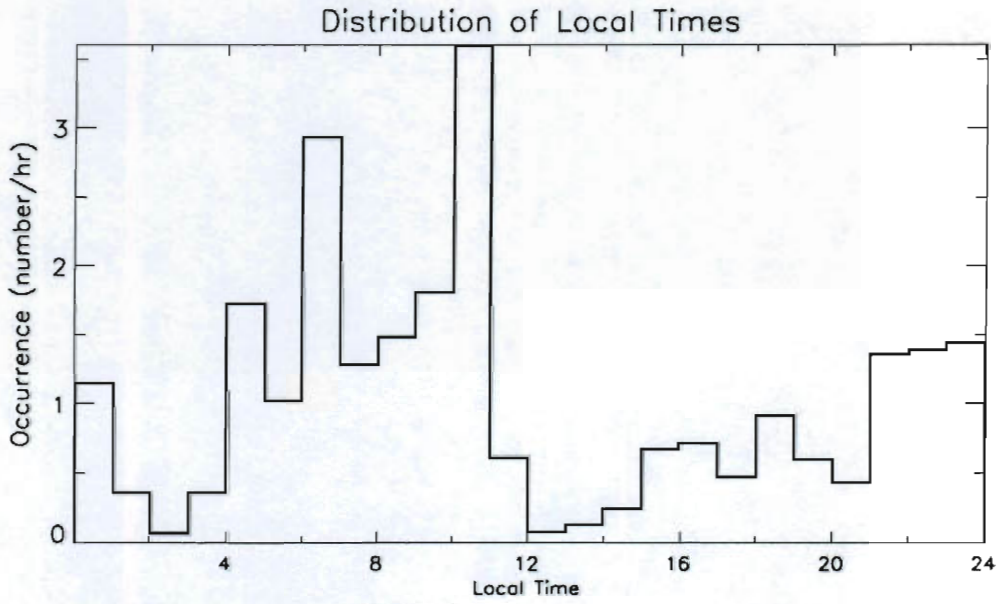

Figure 4.9. Statistical distributions of the injection local times (from *Chen and Hill*, [2008]). Only the 410 events located inside the radial distance range [5,10] are included. Here the vertical axes represent the occurrence frequencies instead of number of events.

Finally, the fraction of the time that is occupied by injection events is calculated for 10° longitude bins. To obtain this fraction for a given longitude sector, we sum over the widths in time of all the events observed in that sector, i.e., the width of one leg of each "V" structure, and divide this by the total time that the spacecraft spent in the same longitude sector in the radial range $5 \leq L \leq 10$. The results are shown in Figure 4.10, where one can see that most values of this fraction are less than 0.1, with a mean value of about 0.05. This gives a sense of the fraction of the available longitude space that is occupied by inflow regions, which is a useful constraint for numerical simulations of the process [e.g., *Wu et al.*, 2007b].

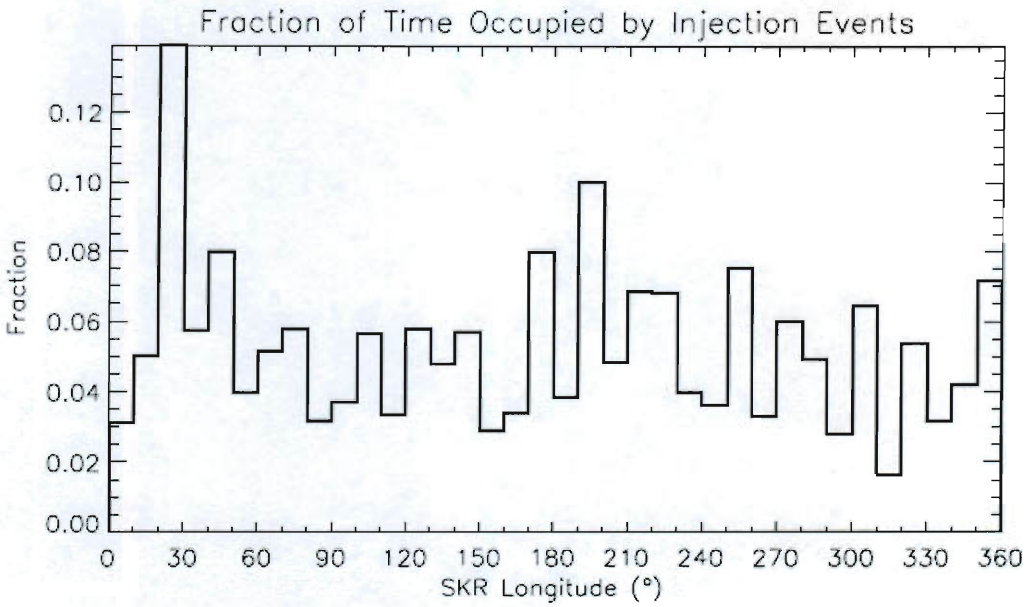

Figure 4.10. Fraction of time occupied by injection events, versus SKR longitude (from *Chen and Hill*, [2008]).

4.5. Periodogram analysis

To further study the possible periodicity of these events, we have done a periodogram analysis, for which we converted our data to a time series. A simple step function was adopted to obtain a time series, with the values set to one inside an injection structure, and zero elsewhere. If there are several injections going on at the same time, we add one to the function's value for each event.

After the time series is obtained, the major problem for a periodicity analysis is the fact that our time series is unevenly spaced. As stated above, we are focusing on the inner part of Saturn's magnetosphere, since most of the events are found when the Cassini spacecraft was in the range $5 \leq L \leq 10$. Our data set has huge gaps when the spacecraft is not in this range. Hence, the commonly-used spectrum techniques such as the Fast Fourier Transform (FFT) are impractical, because the Fourier Transform only works with series that are evenly spaced in time. Instead, we have applied the so-called Lomb-Scargle Algorithm (or the "Lomb periodogram"), which also returns a power spectrum like the FFT, but is designed to handle unevenly spaced data. The Lomb periodogram can test the hypothesis that the time series contains a significant periodic signal by returning a "significance number" with values ranging in the interval [0, 1.0]. The smaller this number is, the more significant the periodic signal is. This algorithm was applied to determine the periods of some other magnetospheric phenomena and has returned favorable outcomes for the magnetic field [*Giampieri et al.*, 2006] and the energetic particles [*Carbary et al.*, 2007a].

There is an existing procedure in the Interactive Data Language (IDL) library which is based on the routine *fasper* from *Press et al.* [1992], named LNP_TEST. After a smoothing and detrending process, this procedure was applied directly. Figure 4.11 shows the normalized power spectrum, where the frequency axis has been converted to time in order to represent the period directly. The most significant feature of this result is its lack of features; instead, a forest of peaks fills the interval between 9.5 hours and 12.5 hours, with no particularly significant peaks that might represent a dominant period in the original data.

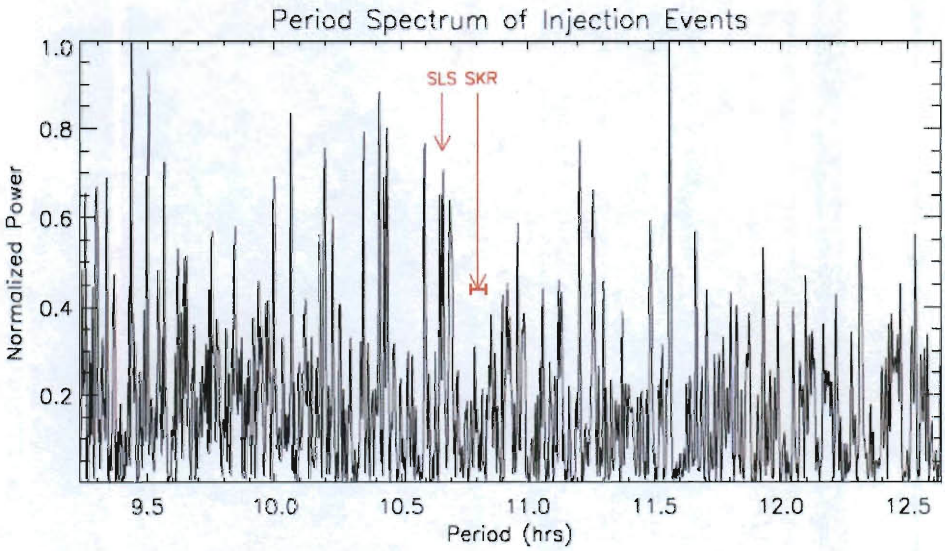

Figure 4.11. Lomb periodogram for all the selected events (from *Chen and Hill*, [2008]). Data have been detrended and smoothed.

4.6. Conclusions

Through the analysis of CAPS electron data, we have compiled statistics of over 400 injection/dispersion events observed during two years of Cassini measurements. The results reported here on the ages and longitude widths are consistent with the previous study [*Hill et al.*, 2005], showing that the injection/dispersion events are mesoscale structures, which typically last several hours. These events are not organized well by the Cassini-era SKR longitude system. Instead, they display a possible modulation at the Voyager-era SLS period, although a periodogram analysis reveals no significant periodicity. The local time distribution reveals a curious asymmetry in which the events tend to cluster in the pre-noon quadrant.

A significant result of our study is that injections occupy a small fraction, ~ 5 - 10%, of the available longitudinal space. This result quantifies the general impression that Saturn's rotation-driven convection system comprises narrow sectors of rapid inflow surrounded by broader regions of slower outflow.

Many injection events have very small ages, as discussed by *Burch et al.* [2005]. These very young events were excluded by the selection criteria in the above study. The data set is expanded to include these young events in the next chapter.

5. Rate of radial transport of plasma in Saturn's inner magnetosphere

In this chapter, we continue our analysis of the injection/dispersion events on the basis of an extended statistical sample space, where we include more young injections that were ruled out before. We assume that the plasma is largely confined to a thin equatorial sheet, and calculate its thickness by deriving the centrifugal scale height profile based on the CAPS observations. We also present the radial and longitudinal dependences of flux tube mass content, as well as the total ion mass between 5 and 10 Saturn radii. Combining these results, we obtain an estimate of the global plasma mass outflow rate in Saturn's inner magnetosphere.

5.1. Introduction

Since the beginning of the Cassini Orbiter mission at Saturn in June 2004, several authors have studied the injection/dispersion events observed in the inner part of the planet's rapidly rotating magnetosphere [e.g., *André et al.*, 2005; *Burch et al.,* 2005; *Hill et al.,* 2005; *Mauk et al.*, 2005]. As we pointed out in the last chapter, these structures emerging in energy-time spectrograms are now widely accepted as direct evidence of inward plasma transport resulting from interchange instabilities that are dynamically dominated by the centrifugal force [e.g., *Hill et al.,* 1981; *Pontius et al.,* 1986]. By analyzing data from the Cassini Plasma Spectrometer (CAPS) [*Young et al.*, 2005], *Chen and Hill* [2008] conducted a statistical study, which included 429 well-shaped injection/dispersion events that were selected from 26 orbits between

July 2004 and August 2006. They obtained results consistent with previous studies with respect to various properties of the injection structures, including their ages, longitudinal widths, and local-time distributions. They reported that no obvious periodicity is present in the occurrence frequency of these events. They further showed that the injection structures occupy only a small fraction (~ 5 - 10%) of the available longitudinal space. This important conclusion implies a picture of Saturn's rotationally driven convection system that comprises narrow rapid inflow channels surrounded by broader but slower outflow channels.

The study described in this chapter continues the analysis of the widths of the injection/dispersion structures, and improves the statistics by extending the sample space to include 622 events including some very young ones as described by *Burch et al.* [2005], which were ruled out by the selection criteria in our previous study. On this basis, the width of inflow and outflow channels in the convection system can be inferred and quantified more accurately.

Wilson et al. [2008] presented profiles of the ion velocity moments within the range 5.5 to 11 R_S (1 R_S = Saturn's equatorial radius = 60,268 km), also on the basis of CAPS observations. We apply these moment data to construct radial profiles of plasma-sheet scale height and flux tube mass content in Saturn's inner magnetosphere. Combining these profiles with our analysis of inflow and outflow channel widths and hence radial speeds, we derive a global estimate of the ion mass

outward transport rate and compare this value with other estimates using different methods.

5.2. Instrumentation and dataset

The Cassini Plasma Spectrometer (CAPS) [*Young et al.,* 2004] includes three sensors, the Electron Spectrometer (ELS), the Ion Mass Spectrometer (IMS) and the Ion Beam Spectrometer (IBS). Together, they provide simultaneous measurements of electrons and positive ions within the energy ranges 0.6 - 28,250 eV and 1 - 49,800 eV respectively, each in 63 contiguous logarithmically spaced energy bins. Both ELS and IMS have eight contiguous detecting anodes arrayed in the elevation direction, each covering 20° of elevation angle. In addition, the whole CAPS instrument is mounted on a rotating actuator, which covers an angular range of up to 208° about the spacecraft Z-axis at a rate ~ $1°s^{-1}$. Thus, CAPS can sample about 56% of the full 4π steradian sky in about three minutes. Additional details of this instrument are described in the Chapter 3.

As discussed by *Hill et al.* [2005] and *Chen and Hill* [2008], these injection/dispersion structures are triggered by the centrifugal interchange instability, which causes the hot, tenuous plasma flux tubes to move inward and exchange with cold, dense flux tubes. The ages of the injections can be inferred from the slopes of the V-shaped features in the spectrograms [equation (1) of *Hill et al.*, 2005]. In these

previous studies we mainly focused on the electron data, because most of the time the rarefied ion distributions produce an IMS counting rate that is too low to reveal the structures. We continue to focus on the ELS data here for the same reason. In addition, we confine our analysis here to the radial distance range 5 - 10 R_S, which is often referred to as Saturn's inner magnetosphere, because most (> 95%) of the injection/dispersion events are observed in this region. One of the selection criteria of *Chen and Hill* [2008] was that the slope of the legs of the V-shaped energy-time dispersion structures must be reliably measurable. This means that very young injections were excluded because the uncertainties of their slopes produce large relative errors in estimating their ages. In this study our focus is not on the ages of the injections, but rather on their widths. Therefore, the very young events are included as long as their widths are reliably identifiable on the time axis. With this change, the total number of injection events in our sample space increases to 622, all from the 27 Cassini orbits between July 2004 and August 2006. The other selection criteria of *Chen and Hill* [2008] are retained. For example, these injection events must be distinguishable from each other, with identifiable apexes of the V-shape structures in the linear scale energy-time spectrograms.

It has long been a difficult problem to calculate reliable ion velocity moments from the CAPS observations because of the instrument's limited and variable field of view. A straightforward numerical integration over observed ion counts produces estimates of ion density, velocity and temperature which are routinely available but frequently suspect because of the incomplete angular coverage [*e.g.*, *Thomsen*, 2009]. *Wilson et*

al. [2008] addressed this problem by applying a forward modeling technique to a carefully selected subset of IMS data between 5.5 and 11 R_S near the day side equatorial plane. On the basis of previous studies [*Young et al.,* 2005], they assumed two ion populations (water group and protons), modeled them as anisotropic Maxwellian distributions with the same bulk flow velocities, and fitted the free parameters to obtain velocity moments for both species. The forward modeling technique places strict requirements on observation conditions, including a favorable field of view and a near-equatorial location, so only 5 orbits (orbits 16, 18, 19, 21, and 23) were selected in their study. Also, interchange injection events were excluded to ensure a roughly constant plasma environment in each data interval. These ion moments are used directly in the following section.

Recent in-flight re-calibration of the CAPS IMS instrument responses (F. J. Crary and D. T. Young, private communication, 2010) indicates a reduction by ~ 30% of the water-group ion densities below ~ 1 keV compared to those reported by *Wilson et al.* [2008]. Thus we have used W^+ density values that are 0.7 times those reported by Wilson et al. This change has no significant effect on the ion velocities and temperatures reported by Wilson et al.

5.3. Results

5.3.1. Widths of injection/dispersion events

The measured partial corotation speed is much larger than the gradient-curvature drift speeds of the particles, and also much larger than the orbital speed of the Cassini spacecraft. When an injection is swept past the spacecraft, the time width Δt of a leg of a V-shaped injection structure can be read directly from a linear energy-time spectrogram. The corresponding longitudinal width W of the structure can then be calculated from

$$W = L R_S \Omega \Delta t . \tag{5.1}$$

Here L represents the dipole L value and Ω is the observed rotational frequency of the sub-corotating plasma, which we take from the polynomial fit to the observed azimuthal velocities in Table 3 of *Wilson et al.* [2008]:

$$V_\phi \text{ (km/s)} = 1.29\left(\frac{R}{R_S}\right)^2 - 12.82\left(\frac{R}{R_S}\right) + 78.56 \tag{5.2}$$

where R represents the planet-centered distance. Because Wilson et al. selected data from equatorial orbits at negligible magnetic latitudes, we can confidently make the approximation $R \approx LR_S$. Figure 5.1 is a scatter plot of the widths of all the events we can identify. The average structure width is calculated for each 0.5 R_S radial bin and is shown by the histogram in Figure 5.1, which shows a modest trend of increasing

width with radial distance. A linear fit is shown by the dashed line in Figure 5.1, the slope of which represents the average angular width of all the injection structures in radians. Our results indicate that this angular width is ~ 2°.

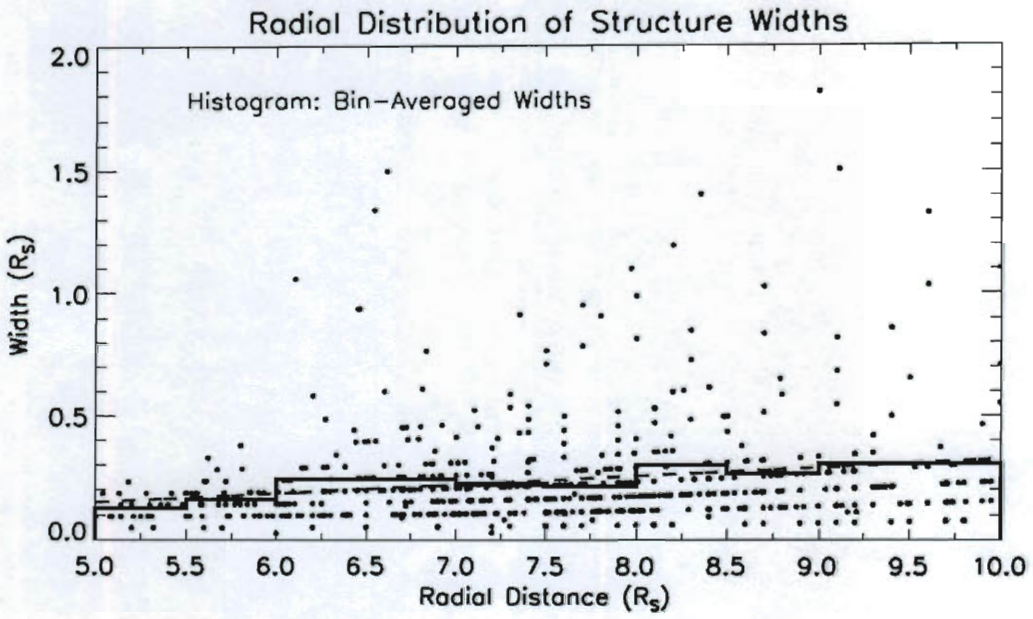

Figure 5.1. Scatter plot of structure widths for all events in our data set (27 orbits, 622 events), from *Chen et al.* [2010]. Histogram shows the average width in each 0.5 R_S radial bin, and the dashed line is the linear fit to the histogram.

To illustrate the relative widths of inflow and outflow sectors we sum over the widths in time of all the injection events in a given longitudinal sector, and divide by the total time that Cassini spent in that sector. We use the Saturn longitude system SLS3 [*Kurth et al.,* 2008], appropriate to this epoch. *Kurth et al.* [2008] also showed that the SLS3 system is equivalent to the SLS2 system we used in our analysis in Chapter 4 (noted as the SKR system there). Using the sub-corotation speeds presented by *Wilson et al.* [2008], we have converted the SLS3 longitudes where the injections were observed to the longitudes where they were injected. Figure 5.2 shows that, on average, only about 7% of the available longitudinal space in our data was occupied by inflow sectors, leaving the rest (~ 93%) for outflow sectors. There is no systematic dependence of this ratio on SLS3 longitude. These results based on our new larger data sample are consistent with those of *Chen and Hill* [2008]. A similar characteristic has been exhibited by numerical simulation results (Figure 5.3) from the Rice Convection Model (RCM) [*e.g., Wu,* 2009; *Liu and Hill,* 2009]. An analysis of the radial dependence of this ratio is shown in Figure 5.4. While there is no obvious dependence on longitude, there is a clear dependence on radial distance, with a broad peak located between 6.5 and 8.5 R_S.

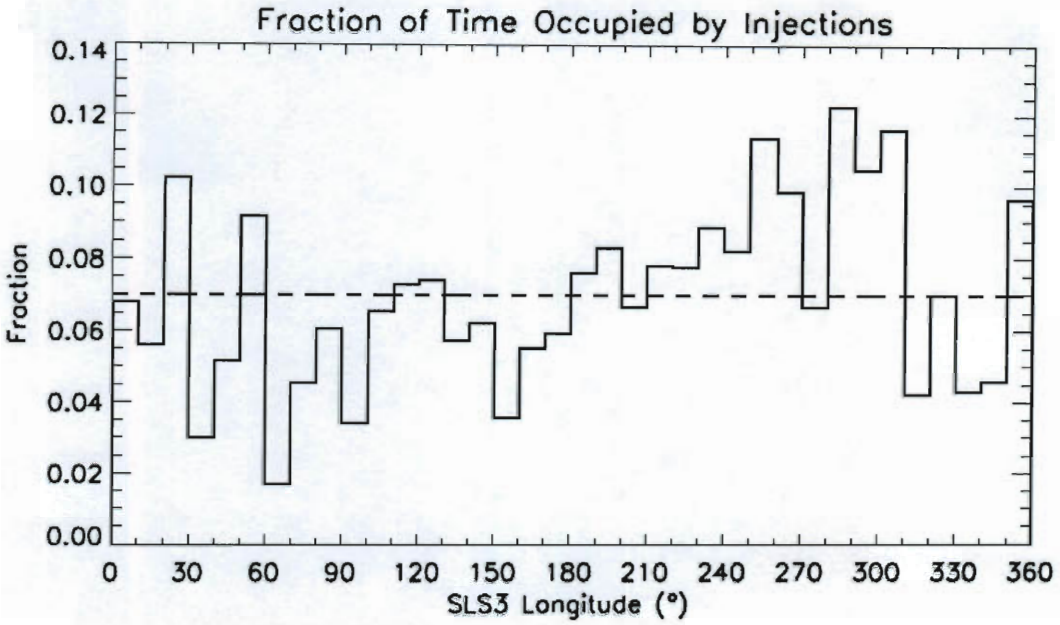

Figure 5.2. Fraction of observation time occupied by plasma inflow channels within 10° SLS3 longitude bins averaged over the radial range 5 – 10 R_S, from *Chen et al.* [2010]. The dashed horizontal line is the longitudinal average.

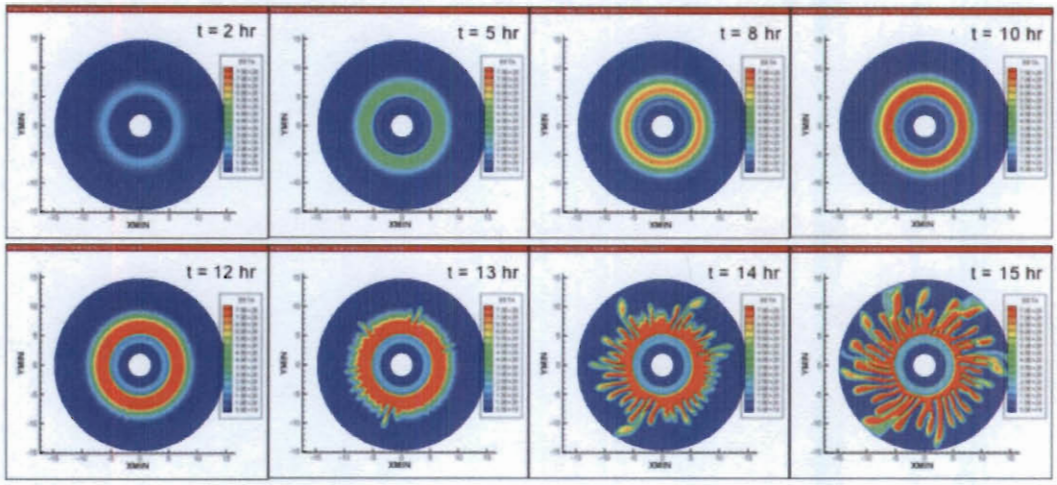

Figure 5.3. RCM simulation of Saturn's magnetospheric convection with active plasma source. Note that the outflow sectors grow wider with time at the expense of the inflow sectors. Note also the relatively stable Enceladus torus at $L \sim 4$ (from *Wu et al.* [2009]).

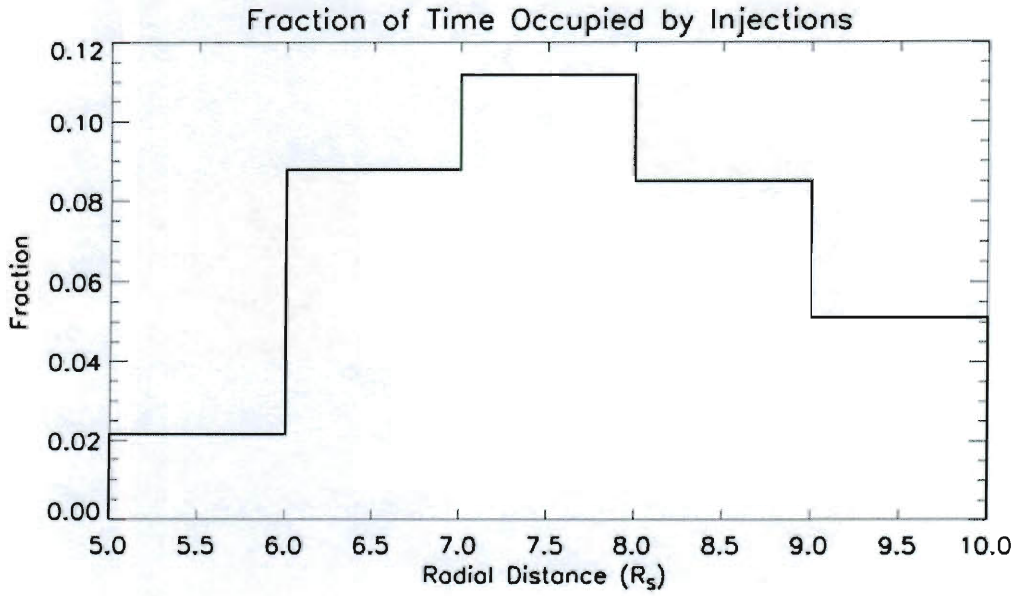

Figure 5.4. Fraction of observation time occupied by plasma inflow channels within 1 R_S radial bins, averaged over SLS3 longitude, from *Chen et al.* [2010].

5.3.2. Centrifugal scale height

In a rotating magnetosphere with dominant internal plasma sources it is expected that plasma is confined in latitude to a region near the spin equatorial plane because of the balance between the pressure gradient force and the centrifugal force [*Hill and Michel,* 1976]. A dense disk-shaped plasma sheet is therefore formed, which, for Saturn, extends from inside 5 R_S to at least 17 R_S [*Bridge et al.,* 1981; *Carbary et al.*, 2008]. The thickness of this sheet is described by the centrifugal scale height [*Hill and Michel,* 1976]

$$H_c = \sqrt{\frac{2k_B T_{//}}{3m_i \Omega^2}} \tag{5.3}$$

where k_B is the Boltzmann constant, $T_{//}$ is the ion parallel temperature, m_i is the average ion mass, and Ω is the observed angular frequency of sub-corotation. *Hill and Michel* [1976] noted that only near-equatorial plasma sources produce strong equatorial confinement of the plasma, a condition that is applicable in Saturn's case where the major plasma source is now known to be the neutral torus produced by the icy satellite Enceladus [e.g., *Johnson et al.,* 2006; *Pontius and Hill,* 2009].

It has been observed that the two dominant ion species in Saturn's inner magnetosphere are water-group ions (W^+) and protons (H^+) [*Young et al.,* 2005]. The density of water group ions is much larger than that of protons ($n_{W^+} / n_{H^+} > 5$) [*Wilson*

et al., 2008, Figure 6 and Table 1]. Moreover, the mass of one water group ion is ~17 times larger than that of a proton. Therefore, we neglect the mass of the protons and only include water group ions in our calculation. We adopt 17 amu as the mean mass of water group ions (m_{W^+}) and use a spin-aligned dipole magnetic field model, since the angle between Saturn's spin axis and magnetic axis is less than 1° [*Smith et al.,* 1980]. Although the dipole field is significantly distorted in the middle magnetosphere [*Khurana et al.,* 2009], the distortion is insignificant, compared to other observational uncertainties, in the inner magnetosphere (5 - 10 R_S), where most of the injections are observed.

Figure 5.5 shows the results of our calculation of the centrifugal scale height, with a fourth-order polynomial fit represented by the solid curve. The half-thickness of the plasma sheet ranges from about 1 to 3 R_S and increases with radial distance between about 6.5 to 9 R_S. This behavior is consistent with that of the electron scale height derived by *Persoon et al.* [2006] from the latitudinal variation of electron densities measured by the RPWS instrument. The results shown here are also consistent with the previous work done by *Rymer et al.* [2009a]. The dip at around 6.5 R_S is directly related to the same feature in the water group ions' parallel temperature profile [*Wilson et al.,* 2008, Figure 7].

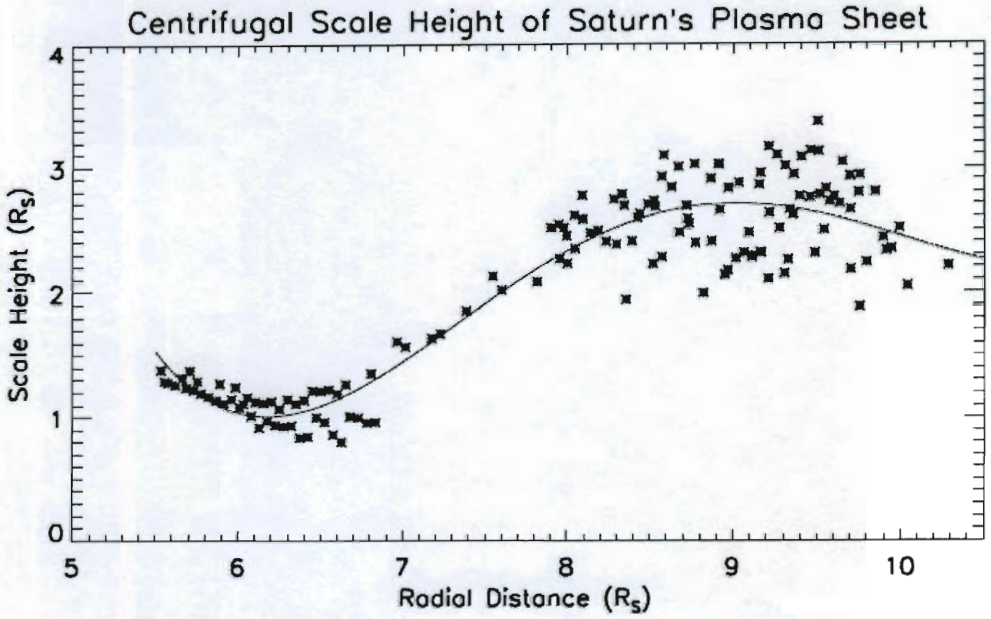

Figure 5.5. Centrifugal scale heights derived from the CAPS ion velocity moments, from *Chen et al.* [2010]. Only water group ions are included; protons are neglected. The solid curve is a fourth-order polynomial fit.

5.3.3. Flux-tube mass content

On the basis of the results above, the column density of the plasma sheet, i.e., the mass of plasma per unit equatorial area, is given by

$$\sigma = 2 n_{W^+} m_{W^+} H_c \tag{5.4}$$

where n_{W^+} and m_{W^+} are the number density and the average mass of water group ions, respectively. The flux-tube mass content can then be calculated from the definition

$$\eta = \frac{\sigma}{B_o L^{-3}} \tag{5.5}$$

where B_0 (0.21×10^{-4} T) is the surface magnetic field strength at Saturn's equator. As in the steps above, our calculation is performed on a point-by-point basis from the data of *Wilson et al.* [2008]. The results are presented in Figure 5.6, where different colors correspond to different orbits of data.

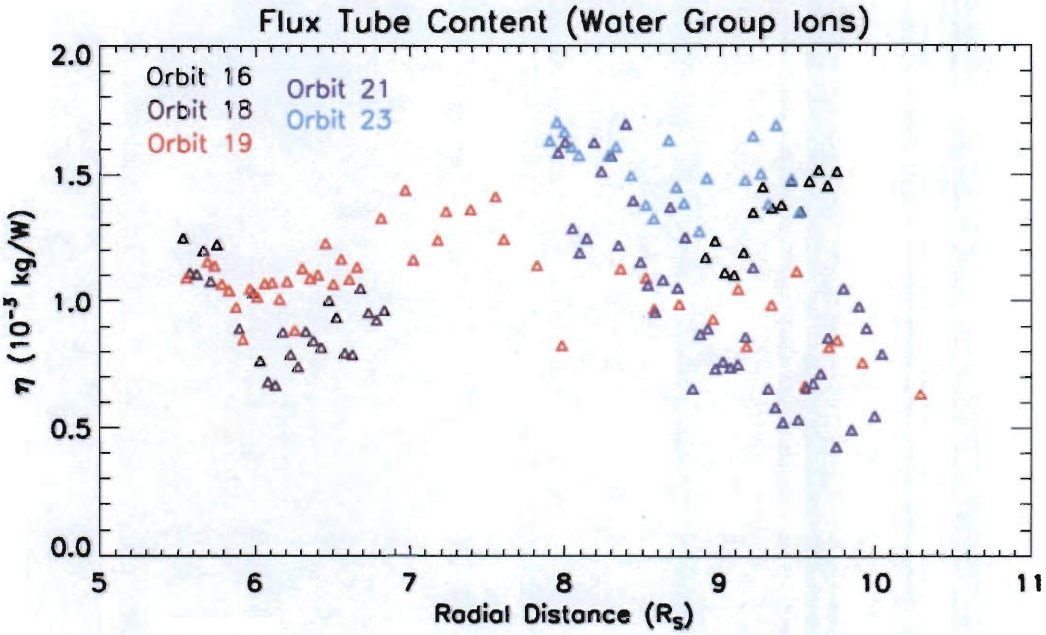

Figure 5.6. Flux tube plasma mass content derived from the CAPS ion velocity moments, neglecting the proton contribution, from *Chen et al.* [2010]. Different colors correspond to the different orbits of data used by *Wilson et al.* [2008].

The flux tube content, in the absence of sources or sinks, would be conserved along streamlines of the flow [e.g., *Hill et al.,* 1981]. Therefore, any radial variations of flux tube content should indicate the existence of plasma mass loading or loss processes. It is obvious from the scatter plot in Figure 5.6 that the flux tube content is not conserved either within an orbit or from orbit to orbit. The values range from about 0.4×10^{-3} to 1.7×10^{-3} kg/Wb with a broad peak located near 8 - 9 R_S. *Rymer et al.* [2008] calculated the total flux tube content to include both water group ions and protons and obtained similar results. It is notable that only one of the five available orbits (orbit 19) covers a relatively complete radial range between 5 and 10 R_S, while the other four orbits of data are quite limited in radial space. We also plot the flux tube content in polar coordinates in Figure 5.7 to show its longitudinal dependence. It is obvious in Figure 5.7 that although the data set of *Wilson et al.* [2008] covers only a limited range of local time, it does cover most SLS3 longitudes. However, the coverage of longitudinal space is still limited within each radial bin, and the flux tube content varies dramatically with longitude in a given radial bin, though not when averaged over radial bins (Figure 5.6). Owing to the limitations of space and time coverage in the observations, the only conclusion that can be safely drawn from Figures 5.6 and 5.7 is that the flux tube content is time variable, both within a given orbit and from one orbit to another.

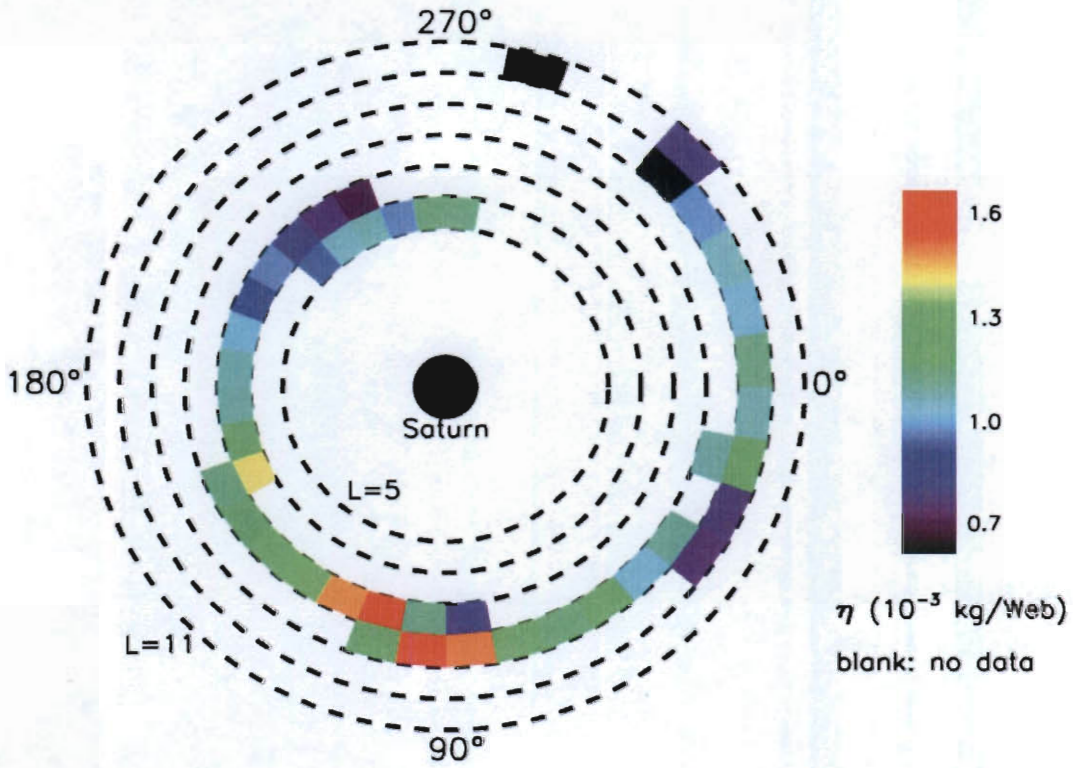

Figure 5.7. The same flux tube contents as in Figure 5.6, shown in polar coordinates (radial distance and SLS3 longitude), from *Chen et al.* [2010]. Concentric dashed circles represent *L*-shells at unit intervals. The color bar represents the magnitude of the average flux tube content in each 1 R_S × 10° bin.

McAndrews et al. [2008] presented additional IMS ion moments outside 10 R_S in the tail region and also derived the flux tube content. In general, their values of η are smaller than those shown here, and show a slight decrease with radial distance, so the radial gradient of flux tube content remains consistently negative outside 10 R_S after its turnover at around 8 - 9 R_S. We do not include these tail data in our study because the injection events are observed mostly inside of 10 R_S.

5.3.4. Mass of inner plasma sheet

With the column mass density (Equation (5.4)), it is straightforward to integrate over radial distance and longitude to obtain the total mass of Saturn's inner plasma sheet. The integral from 5.5 to 10.5 R_S gives a total mass $\sim 5\times10^7$ kg. If we were to count the mass of protons, the result of this estimate would be only slightly larger (< 1%). However, this estimate has considerable (factor ~ 2) error bars because of the limited observational coverage and the approximations made in our calculation. *Rymer et al.* [2007] estimated independently that there are $\sim 2 \times 10^{33}$ charged particles (ions and electrons) in a toroidal region between L=4 and L=10. This is equivalent to a total mass of $\sim 6 \times 10^7$ kg, which is quite consistent with our estimate.

Arridge et al. [2007] used a different method (analysis of observed magnetic perturbations coupled with stress balance arguments) to estimate a total mass $\sim 10^6$ kg for the magnetodisc between 18 and 45 R_S. The difference between our estimate and theirs may indicate a systematic mass loss process between 10.5 and 18 R_S, but it

should be noted that their result was presented only as an order-of-magnitude estimate with large uncertainties, including their assumption of rigid corotation.

5.3.5. Radial speeds of plasma transport

The ratio of the average radial speeds within inflow and outflow sectors at a given distance should be the reciprocal of their average width ratio, because the total potential drop across all inflow and outflow sectors on a given L-shell should be close to zero according to the steady-state version of Faraday's law combined with the ideal MHD condition $\mathbf{E} + \mathbf{v}\times\mathbf{B} = 0$. (This is equivalent to the statement that the magnetic flux contained within a given L shell should be approximately conserved on the time scale of our sampling of a given L shell, i.e., the 10.8-hr rotation period of Saturn [e.g., *Gurnett et al.,* 2005; *Giampieri et al.,* 2006].) We have shown above (Figure 5.2) that the inflow sectors occupy only ~ 7% of the available longitudinal space when averaged over radial distance, so we expect that the average inflow speed should exceed the average outflow speed by a factor ~ (1 – 0.07)/0.07 ~ 13 when averaged over radial distance.

In Figure 5.8, the long dashed histogram shows the radial outflow speeds reported by *Wilson et al.* [2008], averaged over 1 R_S radial bins and then multiplied by a constant factor 5 to make this histogram visually distinguishable from the other histograms shown on the same scale in the same figure. *Wilson et al.* [2008] excluded all injection structures in their study, in order to select relatively time-independent data

intervals necessary to obtain ion velocity moments. Therefore, their V_ρ data only represent the radial speeds within the presumed broad outflow sectors. Figure 10 of *Wilson et al.* [2008] shows that there are both positive and negative V_ρ values in each of our 1-R_S radial bins, in spite of the fact that they excluded inflow sectors by excluding injection/dispersion events. Consistent with this result, numerical RCM simulations [*Liu and Hill,* 2009] exhibit numerous regions of intermittent inward flow embedded within broader regions of global outflow. Owing to statistical undersampling, Figure 10 of *Wilson et al.* [2008] shows essentially zero average outflow speed within our 7 – 8 R_S radial bin; with this exception, there is a clear indication of a roughly linear increase of outflow speed with increasing distance.

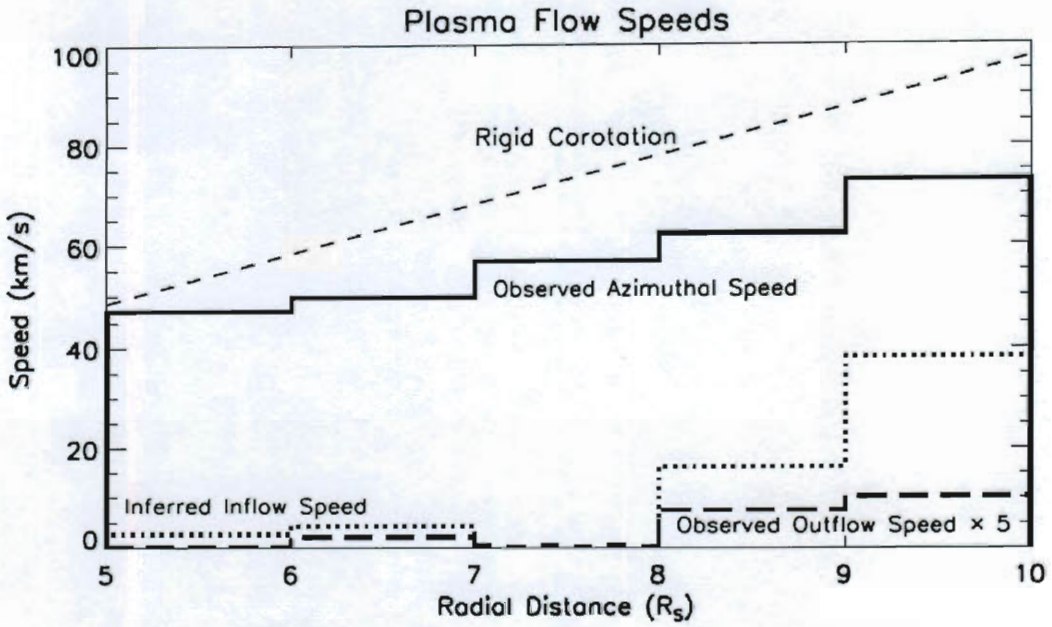

Figure 5.8. Empirical estimates of plasma flow speeds in Saturn's inner magnetosphere, from *Chen et al.* [2010]. The long dashed histogram shows outflow speeds reported by *Wilson et al.* [2008] averaged over 1-R_S radial bins, multiplied by a constant factor of 5 for enhanced visibility. The dotted histogram shows inferred inflow speeds assuming global magnetic flux conservation (see text). The radial bin 7 – 8 R_S is statistically undersampled and shows essentially zero average radial speed both for (measured) outflow and for (inferred) inflow. The solid black histogram shows the azimuthal speeds reported by *Wilson et al.* [2008] averaged within the same radial bins, and the dashed line shows, for reference, the rigid corotation speed.

The dotted histogram in Figure 5.8 shows the bin-averaged inflow speeds inferred from the observed outflow speeds according to the inverse width ratio as described above. With the exception of the same undersampled radial bin noted above (7 – 8 R_S), the inferred inflow speed also increases, faster than linearly, with increasing distance. The figure also shows, for comparison, the observed rotational speeds (the solid black histogram, obtained by averaging the data of Figure 9 of *Wilson et al.* [2008] within the same 1 R_S radial bins), and the ideal rigid corotation speed (dashed black line).

Theoretical considerations (*Vasyliūnas* [1994]; *Hill* [2009]) indicate that in the convection system of a corotation-dominated magnetosphere the radial speed of plasma transport should not exceed the local corotation speed. This sets a theoretical upper limit for both inward and outward transport speeds, which is more restrictive for the former, known to be the larger of the two. The observational results in Figure 5.8 seem to confirm this expectation; both the directly observed outflow speeds and the resultant inferred inflow speeds are uniformly smaller than the local azimuthal speeds, which are in turn uniformly less than the rigid corotation speed.

There are two previous estimates of the inflow speeds of injection structures with which our results can be compared. *Burch et al.* [2005] noted that their observations of a particular (young) injection event are consistent with an average injection speed ~ 25 km/s between 10 and 5 R_S (assuming that speed to be constant within that radial range). This estimate is roughly consistent with our results of Figure 5.8 in the two

radial bins between 8 and 10 R_S. *Rymer et al.* [2009b] estimated from CAPS observations, with a technique very different from ours, a radial injection speed ~ 71 km/s (correcting for an arithmetic error in that paper) between 11 and 7 R_S for a particular injection event that was different from (but similar to) the event considered by *Burch et al.* [2005]. This estimate is outside the range indicated by our statistical results in Figure 5.8.

In addition, we plot the measured radial outflow speeds in a polar coordinate system similar to that of Figure 5.7, and check how they depend on SLS3 longitudes when averaged over each radius bin. The result is shown in Figure 5.9. No obvious pattern can be seen from this figure, except that in the longitude range ~ 270° – 350°, all the measured outflow speeds are negative. But again, this could be due to statistical undersampling. More data is needed and might be available in the future to investigate the correlation between radial outflow speeds and SLS longitudes, if there is any.

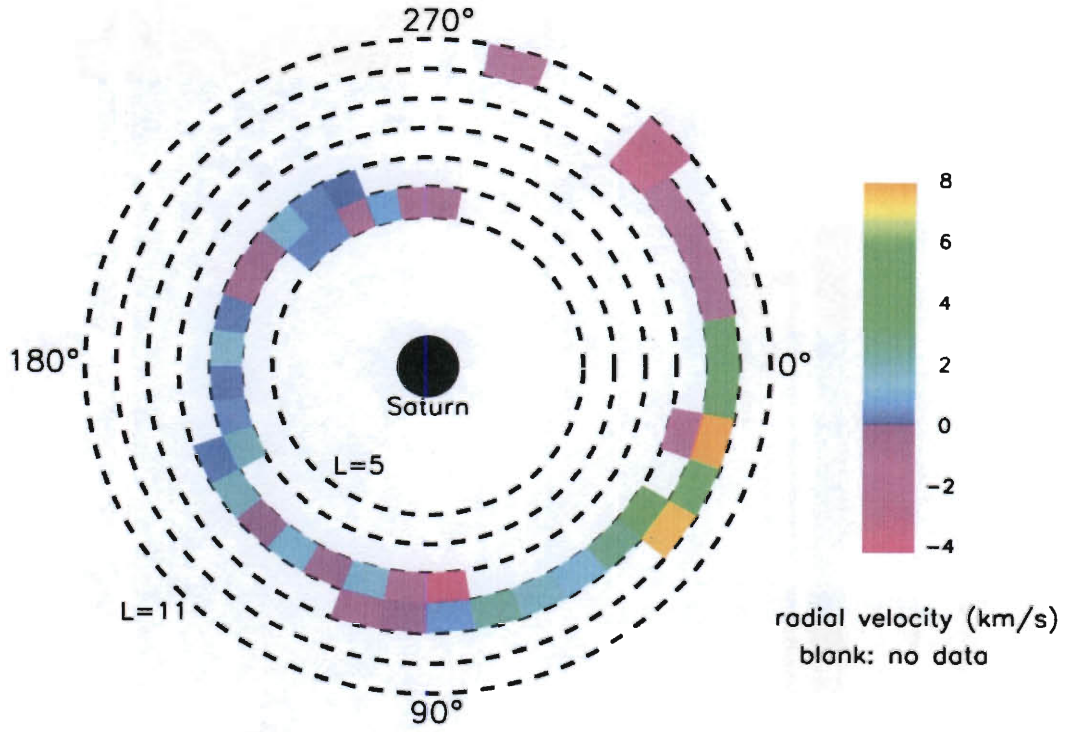

Figure 5.9. Outflow radial velocities measured directly by IMS averaged within each 1 R_S × 10° bin, shown in the same polar coordinate system as in Figure 5.7.

5.3.6. Rate of mass outflow

The ultimate goal of this study is to estimate the global net rate of outward ion mass transport, given by

$$S = S_{out} - S_{in} = \eta_{out}\Phi_{out} - \eta_{in}\Phi_{in} \approx \eta_{out}\Phi_{out} \quad (5.6)$$

where Φ_{out} denotes the potential drop summed over outflow sectors at a given distance, calculated from

$$\Phi_{out} = B_0 L^{-3} V_{out} W_{out} \quad (5.7)$$

where V_{out} is the mean plasma outflow velocity and W_{out} is the mean longitudinal width of outflow channels at a given L-shell, and similarly for Φ_{in}, V_{in} and W_{in}. The approximation in (5.6) follows from the assumption that $\Phi_{out} \approx -\Phi_{in}$ and the observation that $\eta_{out} >> \eta_{in}$.

Before estimating the net mass outflow rate, we first bin the individual measurements of mass outflux by radius and SLS3 longitude. The results are shown in polar coordinates in Figure 5.10, where the color bar represents the mass outflow rate per unit width (i.e., per unit length in the azimuthal direction) at a given L-shell, defined as

$$\frac{d\dot{M}}{dW} = \eta B_0 L^{-3} V_\rho \,. \tag{5.8}$$

Figure 5.10 shows both positive and negative values of $\frac{d\dot{M}}{dW}$, corresponding to positive and negative radial speeds from the IMS observations. However, in general, there are more regions with positive radial flux as expected, consistent with a global picture of broad positive outflow regions. The only radial bin (10 to 11 R_S) that shows only negative radial flux values includes only two data points, which suggests a statistical undersampling. Between longitudes 270° and 310° there is a sector of almost exclusively negative radial flux, but it is uncertain whether this is a persistent longitude pattern or simply an inadequate statistical sampling.

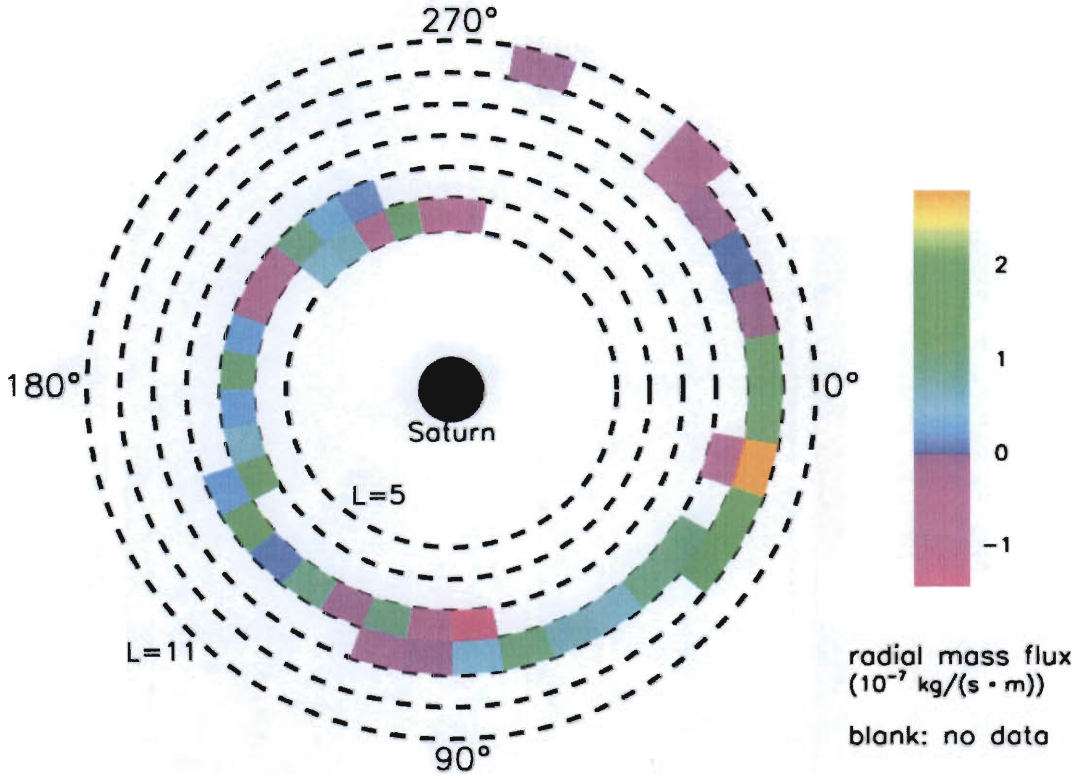

Figure 5.10. Mass outflux per unit width (i.e., per unit length in the azimuthal direction) derived directly from the IMS measured radial velocity components, shown in the same polar coordinate system as in Figure 5.7, from *Chen et al.* [2010].

Finally, we neglect the radial bin 10 to 11 R_S because of its lack of statistical significance, and apply Equations (5.6) and (5.7) to obtain a global estimate of the mass outflow rate versus radial distance. We calculate the azimuthally averaged value of $\frac{d\dot{M}}{dW}$ within a given radial bin, and multiply it by the total width of outflow channels in the same radial bin obtained from Figure 5.4. The results are shown as a histogram in Figure 5.11. Despite the large standard deviations (marked by "error bars") in each radial bin, there is a general trend of increasing bin-averaged mass outflow rate with increasing distance. This feature is qualitatively consistent with the extended plasma source model of *Johnson et al.* [2006]. The magnitude of the global mass outflow rate estimated here is roughly consistent with previous independent order-of-magnitude estimates ~ 100 kg/s obtained from indirect arguments based on CAPS data [*e.g.*, *Tokar et al.*, 2006; *Pontius and Hill*, 2006, 2009].

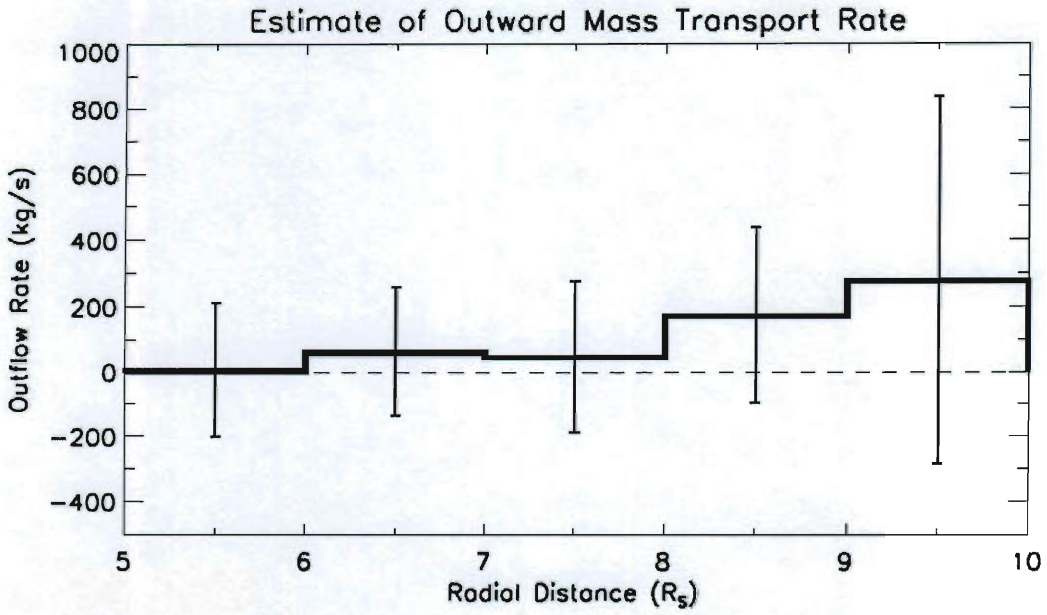

Figure 5.11. Rate of outward transport of ion mass in Saturn's inner magnetosphere, averaged over longitude in each 1 R_S radial bin, from *Chen et al.* [2010]. The "error bar" shown at the center of each bin represents the standard deviation (not the measurement error) of all data points within that bin.

5.4. Conclusions

With an expanded database of injection/dispersion events, we have obtained more complete statistics of the widths of inflow sectors compared with those of outflow sectors in Saturn's inner magnetosphere. When averaged over the radial range 5 to 10 R_S, only ~ 7% of the available longitudinal space is occupied by inflow sectors. This fraction shows no systematic longitudinal dependence but a strong radial dependence, with a broad peak between ~ 6.5 and 8.5 R_S and dropping off sharply outside this range. This result indicates that the radial speed of inflow sectors is, on average, ~ 13 times larger than that of outflow sectors. Both the observed outflow and the inferred inflow speeds are smaller than the local (observed) rotational speeds.

Assuming that the plasma is confined near the equatorial plane, we have calculated the centrifugal scale height of the inner plasma sheet according to the model of *Hill and Michel* [1976]. The resulting scale heights range from about 1 to 3 R_S, with a general tendency to increase with increasing radial distance. The flux tube mass content calculated on this basis is variable both in radial distance and in longitude, probably indicating the existence of variable plasma source or loss processes in the inner magnetosphere. We estimate the total mass of the inner plasma sheet (from 5.5 to 10.5 R_S) to be ~ 5×10^7 kg. We combine our estimate of flux-tube content with IMS observations of radial plasma speeds to obtain a global estimate of the net mass outflow rate ~ 280 kg/s, consistent with but larger than earlier independent estimates.

The prominent increase of mass outflux between 8 and 10 R_S probably indicates extended plasma sources in that region.

If we divide our estimate of the total mass of the plasma sheet between 5 and 10 R_S (5×10^7 kg) by our estimate of 280 kg/s for the mass outflux at 10 R_S, we obtain a plasma residence time ~ 2 days inside 10 R_S. This is interesting: it implies that CAPS sees a totally new plasma sheet on every orbit through Saturn's inner magnetosphere. The neutral water vapor reservoir has a much larger total content, and hence a longer residence time. It therefore acts as a buffer against the radical (order of magnitude) changes in the plasma population that might otherwise be expected from orbit to orbit.

The available determinations of ion velocity moments are very limited, both in time and in space, and we expect that additional measurements in the future will provide us with a more reliable estimate of the mass outflow rate. Additional work is also needed to include the flux tube content profiles inside 5 R_S and outside 10 R_S to provide a more comprehensive picture of mass transport in Saturn's magnetosphere.

6. Discussion

6.1. Additional discussion of the widths of the injections

In Chapters 4 and 5, we have analyzed the widths of the injection events, and obtained a picture of radial convection in Saturn's inner magnetosphere with narrow, fast inflow channels and much broader, slow outflow channels. Here we continue the analysis of the injections' widths.

We have already shown that most of the injections are less than one Saturn radius in width. Meanwhile, the inflow channel width fraction deduced from statistical analysis indicates that only a small portion of available longitude space is occupied by inflow sectors, Figures 5.2 and 5.4 show how this width fraction depends on longitude and radius, respectively. Here we first plot the actual widths of the well-dispersed (old) injection events (described in Chapter 4) with the corresponding SLS3 longitudes (Figure 6.1). It is interesting to note in Figure 6.1 that the inflow channels are wider than average in the longitude range 110° - 140°, which is consistent with the SKR active sector as identified by *Kurth et al.* [2007].

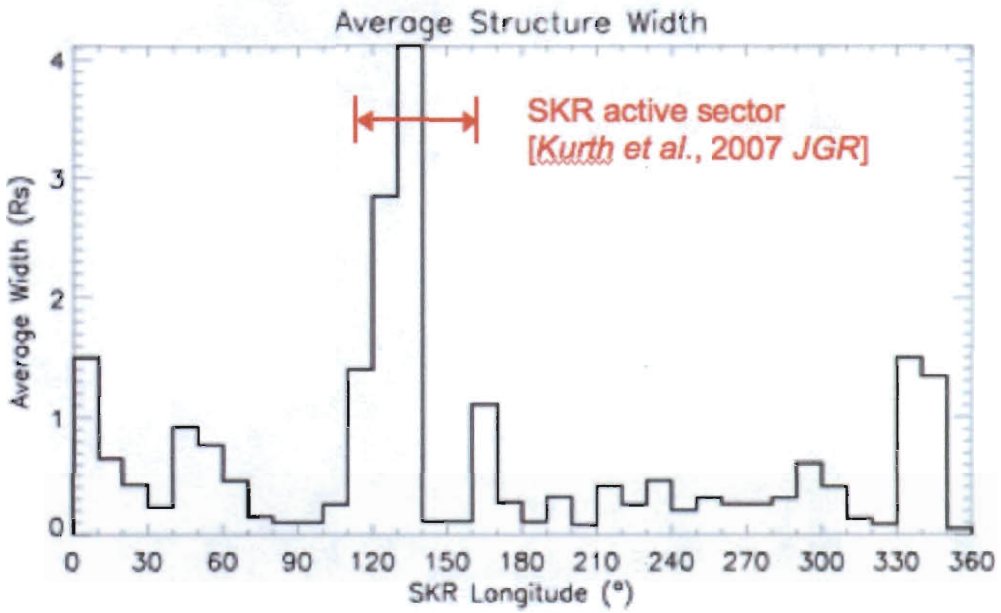

Figure 6.1. Injection widths for the old injections described in Chapter 4, averaged over each 10° SKR (or SLS3) longitude bin.

Moreover, to check whether there exists a specific pattern, we plot the actual inflow sector widths, i.e., the actual angular width of each individual injection event, including the old and young ones, on a polar plot with a coordinate system similar to that of Figure 5.7. The result is presented in Figure 6.2, which shows no obvious pattern except for two very wide injections located in the radius bin 9 – 10 R_S and the two longitude bins 80° – 90° and 120° – 130°.

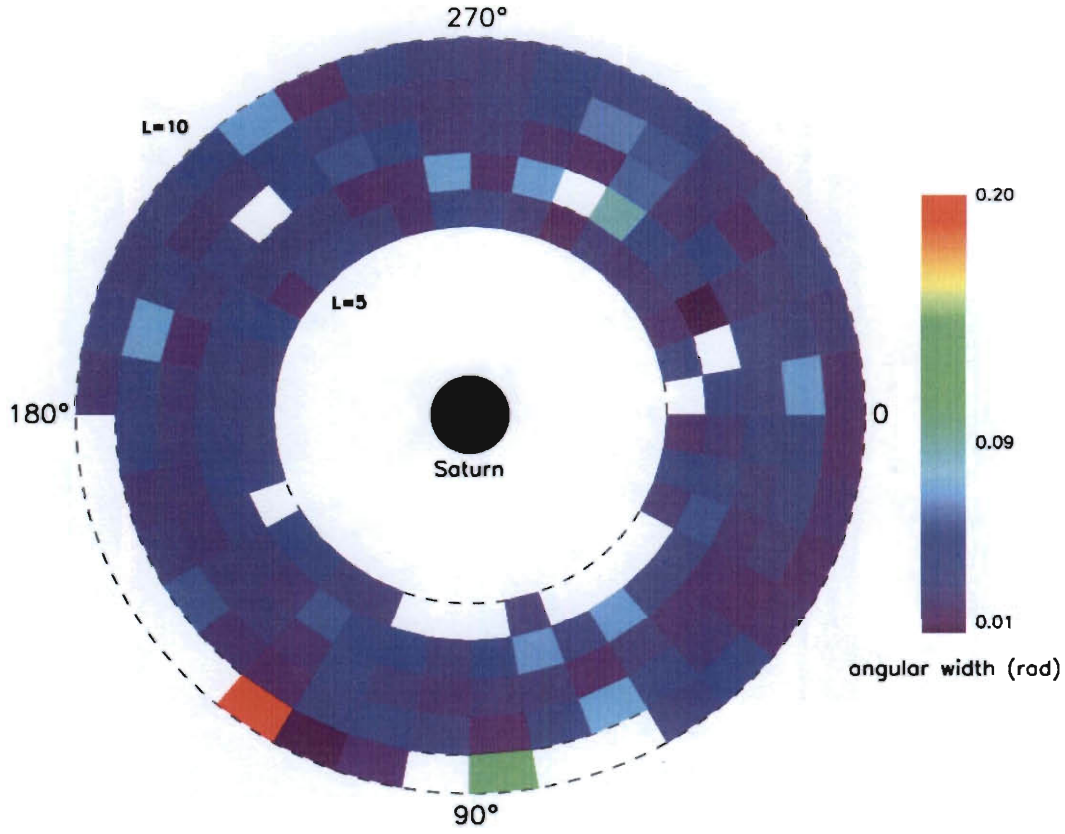

Figure 6.2. Angular width of all the injections in our data set, shown in a coordinate system similar to that of Figure 5.7.

To obtain a better overall view of the distribution pattern we have eliminated these two exceptionally wide injections in Figure 6.3. While no spiral pattern can be detected, and injection widths are randomly distributed in longitude, the radius bin 6 – 7 R_S seems to have more wide injections than other bins.

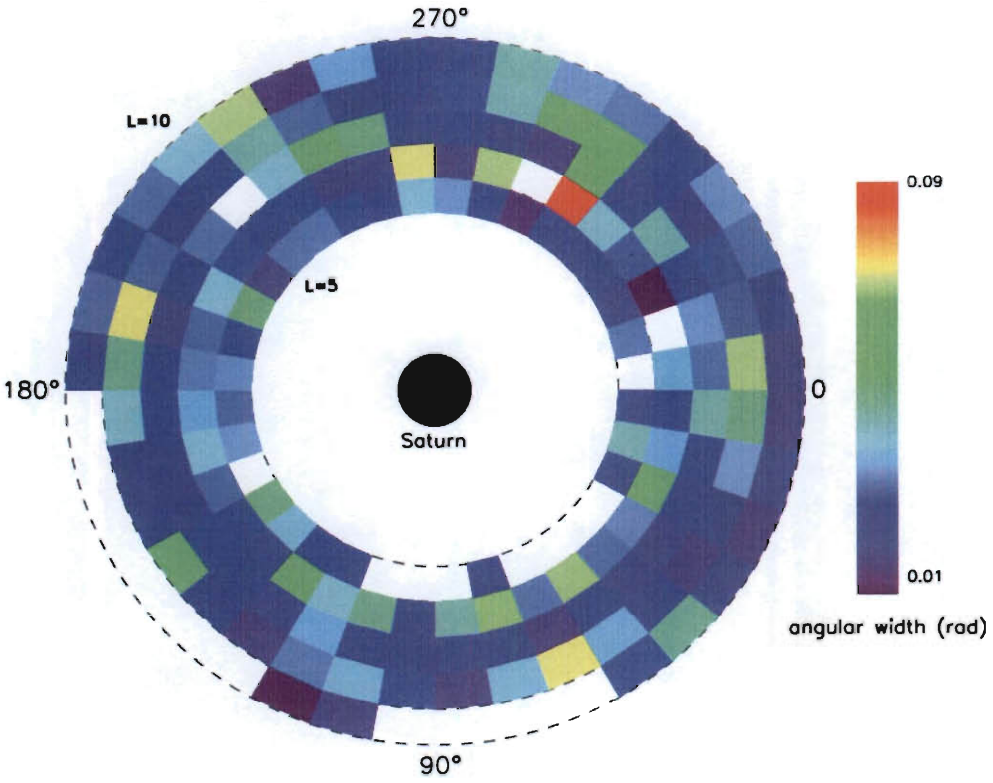

Figure 6.3. Distribution of injection angular widths as in Figure 6.2, but with two exceptionally wide events eliminated.

6.2. Radial speeds of individual injections

We have calculated the individual inward radial speed for each injection flux tube. Recall that *Wilson et al.* [2008] excluded all injection structures in their analysis to obtain ion moments, i.e., their V_ρ data only represent the radial velocities of outflow flux tubes. Therefore, at this time, the inward radial speeds can only be inferred from the relationship between the outward radial speeds and the ratio of inward and outward channels' widths.

In Figure 5.8, we have shown the inferred bin-averaged values of radial inflow speeds. If we multiply these bin-averaged inflow speeds (dotted histogram in Figure 5.8) by the ratio of the average width in that radial bin to the actual width of the individual injection, we can get estimates of the inflow speeds for each injection. The resulting injection speeds are then binned in both longitude and radius, and the result is shown in Figure 6.4. It is clear that the injection speeds increase with radial distance, consistent with the result shown in Figure 5.8. No obvious pattern in longitude can be found here. Again, the extremely low speed values in the radial bin 7 – 8 R_S is caused by the statistical undersampling. Although the average inflow speeds are well below the local corotation speeds, some individual injections have speeds much larger than this limit, which could be caused by measuring errors in reading the injection properties.

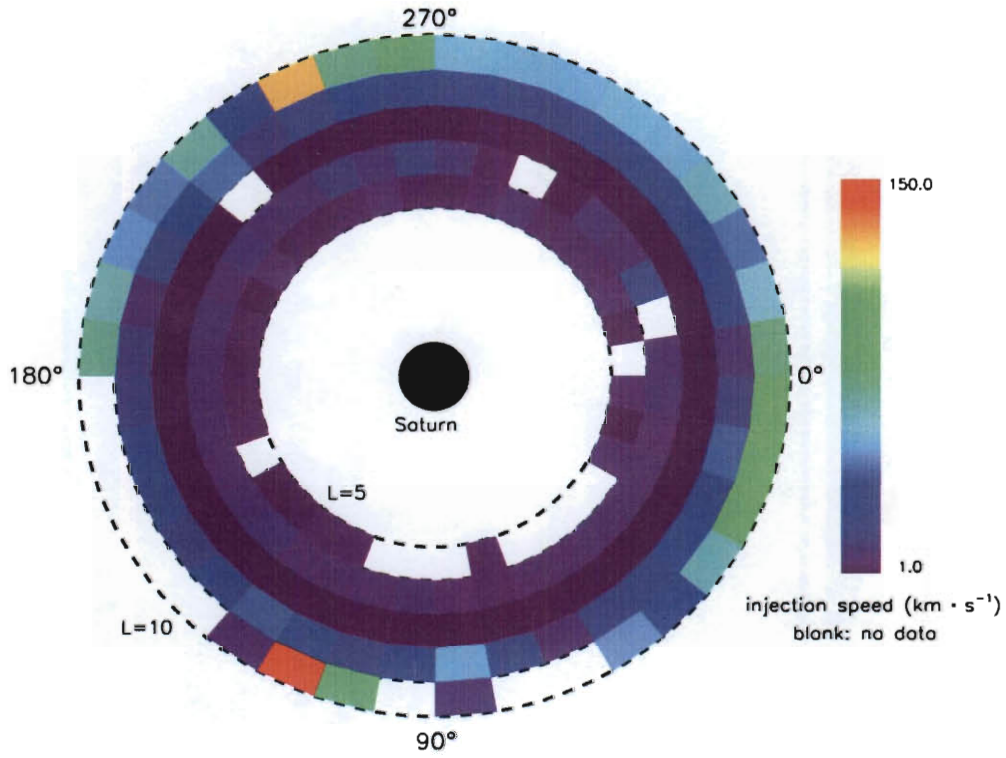

Figure 6.4. Estimated inflow speeds for individual injection events, shown in a coordinate system similar to that of Figure 5.7.

From Figure 6.4 one can see that inflow speeds in the radius bin 9 – 10 R_S and the two longitude bins 110° – 120° and 240° – 250° are particularly large, indeed almost twice the theoretical upper limit imposed by the local azimuthal velocity values. If we remove these two exceptional data points, we obtain the radial speed distribution of individual injections shown in Figure 6.5). Again, no particular pattern can be seen in the figure.

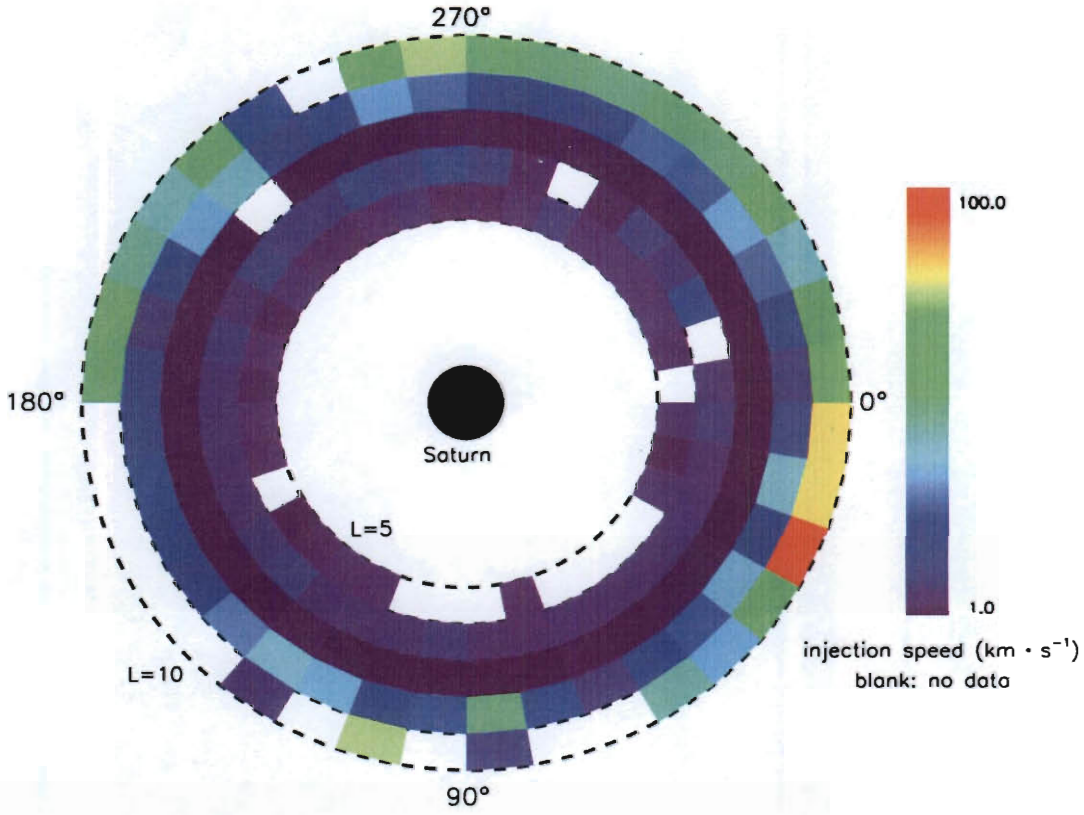

Figure 6.5. Distribution of inflow speeds for individual injections as in Figure 6.4, but excluding two data points with unusually large speed values.

7. Conclusion

In the inner magnetosphere of a rapidly rotating planet such as Jupiter and Saturn, radial transport of plasma mainly comprises hot, tenuous plasma moving inward and cold, denser plasma moving outward. A distinctive phenomenon resulting from the drift dispersion of injecting hot plasma provides direct evidence for this convective motion. Particle instruments aboard the Cassini spacecraft, including the Magnetospheric Imaging Instrument (MIMI) and the Cassini Plasma Spectrometer (CAPS), have made numerous observations of such signatures. These observations provide direct evidence of centrifugally driven plasma transport in Saturn's magnetosphere. In Chapters 4 and 5, we present a series of statistical studies of the properties of such events by analyzing Cassini/CAPS data. A statistical picture of their major characteristics is developed, including the distributions of ages, longitudinal widths, radial distances, and longitudes and local times of injection. The results are basically consistent with those of previous studies [e.g., *Hill et al.*, 2005]. Moreover, an unexpected longitude modulation of these events appears in the old SLS longitude system, which is based on the Saturn kilometric radiation (SKR) observations by Voyager around 1980, while no such modulation seems to exist in the newer SKR longitude systems (SLS2 or SLS3) of the Cassini era. A Lomb periodogram analysis, however, reveals no significant periodic modulation of these events, the reason for which is still unknown and probably needs more work in the future.

In Chapter 4, the injection structures are found to occupy a small fraction (~ 5 – 10%) of the available longitude space. This conclusion is further confirmed in Chapter 5 on the basis of an extended statistical sample of the injection/dispersion events, where we demonstrate that the inflow channels occupy only ~ 7% of the total available longitudinal space. Given the steady-state version of Faraday's law and the ideal MHD condition, this indicates that the inflow speed is much larger than the outflow speed. Through our study, the size of the magnetospheric convection cells is well established, which provides a useful constraint for ongoing numerical studies using the RCM.

Moreover, we assume that the plasma is largely confined to a thin equatorial sheet, and calculate its thickness by deriving the centrifugal scale height profile based on the CAPS/IMS observations. We also present the radial and longitudinal dependences of flux tube mass content, and calculate the total ion mass between 5 and 10 Saturn radii. According to our study, the plasma sheet of Saturn's inner magnetosphere has a north-south thickness of about 2 to 5 R_S, which basically increases with radial distance. The total mass of this inner plasma sheet is of the order of 5×10^7 kg. The measured flux tube content is time variable at the factor-of-two level at a given distance and shows a generally increasing trend with increasing distance. Combining all the results above, we estimate a global plasma mass outflow rate ~ 280 kg/s, which is consistent with but somewhat larger than other independent estimates.

8. Future work

The current work utilized two years data (from July 2004 to August 2006) of CAPS observations to study the injection events in Saturn's inner magnetosphere. We have identified multiple hundreds of events and thus built up a much larger statistical dataset than previous studies. However, with the Cassini spacecraft and the CAPS instrument still working incredibly well currently, more and more data are available to be added to the statistics. It is possible that given a larger sample space, some more distribution features in the radial or longitudinal space might be revealed. Also, it will be very interesting to investigate more on the periodicity information of these injection/events.

As stated in Chapter 5, the reliable ion moments data measured by CAPS using the forward modeling method has been extremely limited both in space and in time. It is expected that more of these measurements will become available in the future, and we might obtain an updated profile of flux tube mass content, thus get a better understanding of the ion loss and source information, as well as a better estimate of the mass outflow rate in Saturn's inner magnetosphere.

It requires strict field of view to measure the inflow velocity directly in a narrow inflow channel. However, if a few of these measurements are achieved, it will be a big step forward for us to constrain more accurately the inflow velocities which were inferred in Chapter 5. We anticipate making more efforts on these and possibly some other aspects (e.g., comparison study between observation and numerical simulation),

in order to understand more about the interesting subject of plasma convection in Saturn's magnetosphere.

Appendix: Relevant basic plasma physics

Plasma, as a distinct state of matter, has different properties from those of solids, liquids, or gases. Although not commonly seen on Earth, over 99% of the visible mass in the universe exists as plasma. For example, the solar wind is essentially a high-speed plasma flow. All the planetary magnetospheres are filled with plasmas. The interactions between planetary magnetospheres and the solar wind occur through plasma interactions.

By definition, a plasma is a collection of a large number of electrically charged particles. The electric charges enable the plasma particles to couple with the electromagnetic field. Because this thesis work is devoted to the study of plasma transport in Saturn's inner magnetosphere, it is appropriate to review some of the basic equations that describe the motion of charged particles in the electromagnetic field.

A.1. Maxwell's equations

Maxwell's equations are the set of four basic equations that mathematically describe of the coupling between the electric field and magnetic field through charge density and current density.

$$\nabla \cdot \vec{E} = \frac{\rho}{\varepsilon_0}, \tag{A.1}$$

$$\nabla \cdot \vec{B} = 0, \tag{A.2}$$

$$\nabla \times \vec{E} = -\frac{\partial \vec{B}}{\partial t}, \tag{A.3}$$

$$\nabla \times \vec{B} = \mu_0 \vec{j} + \mu_0 \varepsilon_0 \frac{\partial \vec{E}}{\partial t}. \tag{A.4}$$

The first equation is Gauss's law, where ε_0 is the vacuum permittivity and ρ is the charge density. Gauss's law describes how the electric field is related to a distribution of electric charges. The second equation, equivalent to Gauss's law for magnetism, states that there exist no "magnetic charges" or magnetic monopoles. The third equation, Faraday's law of induction, states that an electric field can be induced by a time-varying magnetic flux density. Finally, Ampere's law (Equation (A.4)) states that an electric current can generate a magnetic field, where μ_0 is the vacuum permeability and $\vec{j}$ is the current density. The second term on the right hand side of Equation (A.4) is known as the displacement current term, which is negligible as long as there are no fast oscillations in the electric field. Maxwell's equations show that the electric and magnetic fields are not independent of each other.

A.2. Charged particle motion in the electromagnetic field

A charged particle q in an electromagnetic field simultaneously experiences the Coulomb force $q\vec{E}$ and the Lorentz force $q\vec{v} \times \vec{B}$. Given m as the mass of this particle and $\vec{v}$ as the particle velocity, its motion can be described by

$$\vec{F} = m\frac{d\vec{v}}{dt} = q\left(\vec{E} + \vec{v} \times \vec{B}\right). \tag{A.5}$$

The Lorentz force is always perpendicular to the particle's velocity, and thus causes the particle's gyromotion (i.e., cyclotron gyration) around the magnetic field lines. The center of the gyration is called the guiding center. The gyroradius (also called Larmor radius) is

$$r_L = \frac{m v_\perp}{|q| B} \tag{A.6}$$

where $v_\perp$ is the velocity component perpendicular to the magnetic field. The gyrofrequency, or cyclotron frequency, depends on the sign of the charge:

$$\omega_c = \frac{qB}{m}. \tag{A.7}$$

The existence of an electric field will add another component to the particle's motion, namely, the $\vec{E} \times \vec{B}$ drift motion, which has the general form

$$\vec{v}_E = \frac{\vec{E} \times \vec{B}}{B^2}. \tag{A.8}$$

Note that the direction of the $\vec{E} \times \vec{B}$ drift motion is independent of the sign of the charge, i.e., positive ions and electrons move in the same direction.

In addition to the Coulomb force, any general external force $\vec{F}$ acting on a charged particle in the magnetic field can cause a drift motion perpendicular to the field lines. Equation (A.8) can be generalized to the form

$$\vec{v}_d = \frac{1}{q}\frac{\vec{F} \times \vec{B}}{B^2} = \frac{1}{\omega_c}\frac{\vec{F} \times \vec{B}}{mB}. \tag{A.9}$$

Therefore, except for the Coulomb force, a general force, e.g., gravity, causes electrons and positive ions to drift in opposite directions, and thus leads to the separation of charges with different signs.

Two kinds of drift motions caused by a non-uniform magnetic field, namely gradient drift and curvature drift, are directly related to our work described above. The force that a particle experiences due to the gradient of magnetic field can be expressed as

$$\vec{F}_{\nabla} = -\mu \nabla B \tag{A.10}$$

where $\mu = \frac{m v_{\perp}^{2}}{2B}$ is the magnetic moment. When the field lines are curved, a particle with a parallel velocity component $v_{//}$ experiences the centrifugal force

$$\vec{F}_{R} = m v_{//}^{2} \frac{\vec{R}_{c}}{R_{c}^{2}}. \tag{A.11}$$

Inserting these two force expressions into Equation (A.9) gives the standard expressions for gradient and curvature drift velocities.

References

André, N., M. K. Dougherty, C. T. Russell, J. S. Leisner, and K. K. Khurana (2005), Dynamics of the Saturnian inner magnetosphere: first inferences from the Cassini magnetometers about small-scale plasma transport in the magnetosphere, *Geophys. Res. Lett.*, 32, L14S06, doi:10.1029/2005GL022643.

Arridge, C. S., C. T. Russell, K. K. Khurana, N. Achilleos, N. André, A. M. Rymer, M. K. Dougherty, and A. J. Coates (2007), Mass of Saturn's magnetodisc: Cassini observations, *Geophys. Res. Lett.*, 34, L09108, doi:10.1029/2006GL028921.

Brice, N. M., Ioannidis, G.A. (1970), The magnetospheres of Jupiter and Earth, *Icarus*, 13 (2), pp. 173-183.

Bridge, H. S., *et al.* (1981), Plasma observations near Saturn: initial results from Voyager 1, *Science,* 212, 217, doi: 10.1126/science.212.4491.217.

Burch, J. L., J. Goldstein, T. W. Hill, D. T. Young, F. J. Crary, A. J. Coates, N. Andre, W. S. Kurth, and E. C. Sittler Jr. (2005), Properties of local plasma injections in Saturn's magnetosphere, *Geophys. Res. Lett.*, 32, L14S02, doi:10.1029/2005GL022611.

Carbary, J. F., D. G. Mitchell, S. M. Krimigis, D. C. Hamilton, and N. Krupp (2007a), Charged particle periodicities in Saturn's outer magnetosphere, *J. Geophys. Res.*, 112, A06246, doi:10.1029/2007JA012351.

Carbary, J. F., D. G. Mitchell, S. M. Krimigis, and N. Krupp (2007b), Evidence for spiral pattern in Saturn's magnetosphere using the new SKR longitudes, *Geophys. Res. Lett.*, 34, L13105, doi:10.1029/2007GL030167.

Carbary, J. F., D. G. Mitchell, C. Paranicas, E. C. Roelof, and S. M. Krimigis (2008), Direct observation of warping in the plasma sheet of Saturn, *Geophys. Res. Lett.*, 35, L24201, doi:10.1029/2008GL035970.

Chen, C. -K. (1977), *Topics in planetary plasmaspheres*, Ph. D. thesis, University of California, Los Angeles, California, USA.

Chen, Y., and T. W. Hill (2008), Statistical analysis of injection/dispersion events in Saturn's inner magnetosphere, *J. Geophys. Res.*, 113, A07215, doi:10.1029/2008JA013166.

Chen, Y., T. W. Hill, A. M. Rymer, and R. J. Wilson (2010), Rate of radial transport of plasma in Saturn's inner magnetosphere, *J. Geophys. Res.*, in press.

Cowley S. W. H., D. M. Wright, E. J. Bunce, A. C. Carter, M. K. Dougherty, G. Giampieri, J. D. Nichols, and T. R. Robinson (2006), Cassini observations of planetary-period magnetic field oscillations in Saturn's magnetosphere: Doppler shifts and phase motion, *Geophys. Res. Lett.*, 33, L07104, doi:10.1029/2005GL02552.

Dessler, A. J. (1980), Corotating Birkeland currents in the Jovian magnetosphere: an Io plasma-torus source. *Planet. Space Sci.* 28 (1980), pp. 781–788.

Dessler, A. J., B. R. Sandel, and S. K. Atreya (1981), The Jovian hydrogen bulge: Evidence for co-rotating magnetospheric convection, *Planet. Space Sci.*, 29, 215, 1981.

Dougherty, M., K. (2001), Saturn: Magnetosphere, *Encyclopedia of Astronomy and Astrophysics*, ed. E. Priest, 3, 2361-2367, 2001.

Dungey, J. W. (1961), Interplanetary magnetic field and the auroral zones, *Phys. Rev. Lett.*, 6, 47–48.

Espinosa, S. A., D. J. Southwood, and M. K. Dougherty (2003), How can Saturn impose its rotation period in a noncorotating magnetosphere?, *J. Geophys. Res.*, *108*, 1086, doi:10.1029/2001JA005084.

Giampieri, G., M. K. Dougherty, E. J. Smith, and C. T. Russell (2006), A regular period for Saturn's magnetic field that may track its internal rotation, *Nature, 441*, 62– 64, doi:10.1038/nature04750.

Gold, T. (1959), Motions in the magnetosphere of the Earth, *J. Geophys. Res.*, 64, 1219.

Gurnett, D. A., el al. (2004), The Cassini radio and plasma wave investigation, *Space Sci. Rev.*, 114,395-463.

Gurnett, D. A., et al. (2005), Radio and plasma wave observations at Saturn from Cassini's approach and first orbit, *Science, 307,* 1255 – 1259, doi:10.1126/science.1105356.

Gurnett, D. A., A. M. Persoon, W. S. Kurth, J. B. Groene, T. F. Averkamp, M. K. Dougherty, and D. J. Southwood (2007), The variable rotation period of the inner region of Saturn's plasma disk, *ScienceExpress*, doi:10.1126/science.1138562.

Hill, T. W., and F. C. Michel (1976), Heavy ions from the Galilean satellites and the centrifugal distortion of the Jovian magnetosphere, *J. Geophys. Res.*, 81(25), 4561–4565.

Hill, T. W. (1976), Interchange stability of a rapid rotating magnetosphere, *Planet. Space Sci.*, 24, 1151-1154.

Hill, T. W. (1979), Inertial limit on corotation, *J. Geophys. Res.,* 84, 6554-6558, doi:10.1029/JA084iA11p06554.

Hill, T. W., A. J. Dessler, and L. J. Maher (1981), Corotating magnetospheric convection, *J. Geophys. Res.*, 86(A11), 9020–9028.

Hill, T. W. (1983), Solar-wind magnetosphere coupling, in *Solar-Terrestrial Physics*, (R. L. Carovillano and J. M. Forbes, ed.) D. Reidel, Boston, MA, pp. 261-302.

Hill, T. W., A. J. Dessler, and C. K. Goertz (1983), Magnetospheric models, in *Physics of the Jovian Magnetosphere*, edited by A. J. Dessler, chap. 11, p. 395, Cambridge Univ. Press, New York.

Hill, T. W. (1984), Saturn's E rings, *Adv. Space Res.* **4** (1984), pp. 149–157.

Hill, T. W., and A. J. Dessler (1991), Plasma motions in planetary magnetospheres, *Science,* 252, 410-415.

Hill, T. W., A. M. Rymer, J. L. Burch, E. J. Crary, D. T. Young, M. F. Thomsen, D. Delapp, N. Andre, A. J. Coates, and G. R. Lewis (2005), Evidence for rotationally driven plasma transport in Saturn's magnetosphere, *Geophys. Res. Lett.*, 32,L14S10, doi:10.1029/2005GL022620.

Hill, T. W. (2009), Speed limit for centrifugally driven convection, *EOS Trans. AGU, 90*(52), Fall Meet. Suppl., Abstract SM31D-08.

Johnson, R. E., H. T. Smith, O. J. Tucker, M. Liu, M. H. Burger, E. C. Sittler, and R. L. Tokar (2006), The Enceladus and OH tori at Saturn, *Astrophys. J.,* 644, L137–L139.

Khurana, K. K., D. G. Mitchell, C. S. Arridge, M. K. Dougherty, C. T. Russell, C. Paranicas, N. Krupp, and A. J. Coates (2009), Sources of rotational signals in

Saturn's magnetosphere, *J. Geophys. Res.*, 114, A02211, doi:10.1029/2008JA013312.

Krimigis, S. M., et al. (2005), Dynamics of Saturn's magnetosphere from MIMI during Cassini's orbital insertion, *Science*, 307, 1270.

Kurth, W. S., A. Lecacheux, T. F. Averkamp, J. B. Groene, and D. A. Gurnett (2007), A Saturnian longitude system based on a variable kilometric radiation period, *Geophys. Res. Lett.*, 34, L02201, doi:10.1029/2006GL028336.

Kurth, W. S., T. F. Averkamp, D. A. Gurnett, J. B. Groene, and A. Lecacheux (2008), An update to a Saturnian longitude system based on kilometric radio emissions, *J. Geophys. Res.*, 113, A05222, doi:10.1029/2007JA012861.

Liu, X., and T. W. Hill (2009), Analysis of RCM simulations of plasma transport in Saturn's inner magnetosphere, *EOS Trans. AGU*, *90*(52), Fall Meet. Suppl., Abstract SM23C-1627.

Mauk, B. H., D. J. Williams, and R. W. McEntire (1997), Energy-time dispersed charged particle signatures of dynamic injections in Jupiter's inner magnetosphere, *Geophys. Res. Lett.*, 24, 2949.

Mauk, B. H., et al., (1999), Storm-like dynamics of Jupiter's inner magnetosphere, *J. Geophys. Res.*, 104, 22,759

Mauk, B. H., et al., (2005), Energetic particle injections in Saturn's magnetosphere, *Geophys. Res. Lett.*, 32, L14S05, doi:10.1029/2005GL022485.

Mauk, B. H., D. Hamilton, T. W. Hill, G. Hospodarsky, R. E. Johnson, C. Paranicas, E. Roussos, C. T. Russell, D. Shemansky, E. Sittler, and R. M. Thorne (2009), Fundamental plasma processes in Saturn's magnetosphere, in *Saturn from*

Cassini-Huygens, edited by M. Dougherty, L. Esposito, and S. M. Krimigis, Springer Verlag, Dordrecht.

McAndrews, H. J., *et al.* (2009), Plasma in Saturn's nightside magnetosphere and the implications for global circulation, *Planet. Space Sci.*, doi:10.1016/j.pss.2009.03.003.

Melrose, D.B. (1967), Rotational effects on the distribution of thermal plasma in the magnetosphere of Jupiter, *Planet. Space Sci.*, 15 (2), pp. 381-393.

Persoon, A. M., D. A. Gurnett, W. S. Kurth, and J. B. Groene (2006), A simple scale height model of the electron density in Saturn's plasma disk, *Geophys. Res. Lett.*, 33, L18106, doi:1029/2006GL027090.

Pontius, D. H., Jr., T. W. Hill, and M. E. Rassbach (1986), Steady state plasma transport in a corotation-dominated magnetosphere, *Geophys. Res. Lett.*, 13,1097.

Pontius, D. H., Jr., and T. W. Hill (1989), Rotation Driven Plasma Transport: The Coupling of Macroscopic Motion and Microdiffusion, *J. Geophys. Res.*, 94(A11), 15,041–15,053.

Pontius, D. H., Jr., and T. W. Hill (2006), Enceladus: A significant plasma source for Saturn's magnetosphere, *J. Geophys. Res.*, 111, A09214, doi:10.1029/2006JA011674.

Pontius, D. H., Jr., and T. W. Hill (2009), Plasma mass loading from the extended neutral gas torus of Enceladus as inferred from the observed plasma corotation lag, *Geophys. Res. Lett.*, **36**, L23103, doi:10.1029/2009GL041030.

Porco, C. C., et al., (2006), Cassini observes the active south pole of Enceladus, *Science,* 311, 1393-1401.

Press, W.H., S. A. Teukolsky, W. T. Vetterling, and B. P. Flannery (1992), *Numerical Recipes: the Art of Scientific Computing*, Cambridge Univ. Press, Cambridge, England, pp. 569-577.

Rymer, A. M., et al. (2007), Electron sources in Saturn's magnetosphere, *J. Geophys. Res.*, 112, A02201, doi:10.1029/2006JA012017.

Rymer, A. M.; Mauk, B. H.; Paranicas, C.; Hill, T. W.; Sergis, N.; Schippers, P.; Young, D. T. (2008), Plasma Injection and Circulation at Saturn, *Eos Trans. AGU*, 89(23), Jt. Assem. Suppl., Abstract SM43B-05.

Rymer A.M., B.H. Mauk and T. W. Hill (2009a), Why is Radial Transport of Plasma at Saturn Asymmetric?, *Eos Trans. AGU*, 90(22), Jt. Assem. Suppl., Abstract SM13A-04.

Rymer, A. M., B. H. Mauk, T. W. Hill, N. André, D. G. Mitchell, C. Paranicas, D. T. Young, H. T. Smith, A. M. Persoon, J. D. Menietti, G. B. Hospodarsky, A. J. Coates, and M. K. Dougherty (2009b), Cassini evidence for rapid interchange transport at Saturn, *Plan. Space Sci.*, doi:10.1016/j.pss.2009.04.010.

Seidelmann, P. K., et al. (2002), Report of the IUA/IAG working group on cartographic coordinates and rotational elements of the planets and satellites:2000, *Celestial Mech. Dyn. Astron.*, 82, 83-110.

Siscoe, G. L., and D. Summers (1981), Centrifugally driven diffusion of Iogenic plasma, *J. Geophys. Res.*, 86(A10), 8471.

Smith, E. J., *et al.*, (1980), Saturn's magnetic field and magnetosphere, *Science,* 207, 407, doi:10.1126/science.207.4429.407.

Sonnerup, B. U. Ö., and M. J. Laird (1963), On magnetospheric interchange instability, *J. Geophys. Res.*, 68(1), 131.

Thomsen, M. F. (2009), Overview of Cassini CAPS observations of thermal plasma in Saturn's magnetosphere, *EOS Trans. AGU*, *90*(52), Fall Meet. Suppl., Abstract SM31D-02.

Tokar, R. L., R. E. Johnson, T. W. Hill, D. H. Pontius, W. S. Kurth, F. J. Crary, D. T. Young, M. F. Thomsen, D. B. Reisenfeld, A. J. Coates, G. R. Lewis, E. C. Sittler, and D. A. Gurnett (2006), The interaction of the atmosphere of Enceladus with Saturn's plasma, *Science*, **311**, 1409, doi: 10.1126/science.1121061.

Vasyliūnas, V. M. (1978), A mechanism for plasma convection in the inner Jovian magnetosphere (abstract), STP Symposium, Book of Abstracts, Innsbruck, Austria, June 1978.

Vasyliūnas, V. M. (1983), Plasma distribution and flow, in *Physics of the Jovian Magnetosphere*, edited by A. J. Dessler, chap. 11, p. 395, Cambridge Univ. Press, New York.

Vasyliūnas, V. M. (1989), Maximum scales for preserving flux tube content in radial diffusion driven by interchange motions, *Geophys. Res. Lett.*, *16*, 1465.

Vasyliūnas, V. M. (1994), Role of the plasma acceleration time in the dynamics of the Jovian magnetosphere, *Geophys. Res. Lett.*, *21*, 401-404.

Vasyliūnas, V. M. (2008), Comparing Jupiter and Saturn: dimensionless input rates from plasma sources within the magnetosphere, *Ann. Geophys.*, 26, 1341–1343.

Waite, H. J. Jr., et al. (2006), Cassini ion and neutral mass spectrometer: Enceladus plume composition and structure, *Science*, 311, 1419–1422, doi:10.1126/science.1121290.

Wilson, R. J., R. L. Tokar, M. G. Henderson, T. W. Hill, M. F. Thomsen, and D. H. Pontius Jr. (2008), Cassini plasma spectrometer thermal ion measurements in Saturn's inner magnetosphere, *J. Geophys. Res.*, 113, A12218, doi:10.1029/2008JA013486.

Wilson, R. J., R. L. Tokar, M. G. Henderson, M. F. Thomsen, D. H. Pontius, and T. W. Hill (2007), Thermal plasma flow in Saturn's inner magnetosphere, *EOS Trans. AGU*, *88*(52), Fall Meet. Suppl., Abstract P43A-1020.

Wolf R. A. (1995), *Physics of the magnetosphere,* course notes, Rice University, Houston, Texas, USA.

Wu, H., T. W. Hill, R. A. Wolf, and R. W. Spiro (2007a), Numerical simulation of fine structure in the Io plasma torus produced by the centrifugal interchange instability, *J. Geophys. Res.*, 112, A02206, doi:10.1029/2006JA012032.

Wu, H., T. W. Hill, R. A. Wolf, and R. W. Spiro (2007b), Numerical simulation of Coriolis effects on the interchange instability in Saturn's magnetosphere, *EOS Trans.* AGU, *88*(52), Fall Meet. Suppl., Abstract P43A-1006.

Wu, H., (2009), *Rice Convection Model Simulations of the Centrifugal Interchange Instability in the Magnetospheres of Jupiter and Saturn*, Ph. D. Thesis, Rice University, Houston, Texas, USA.

Xing, X., and R. A. Wolf (2007), Criterion for interchange instability in a plasma connected to a conducting ionosphere, *J. Geophys. Res.*, 112, A12209, doi:10.1029/2007JA012535.

Yang, Y. S., R. A. Wolf, R. W. Spiro, T. W. Hill, and A. J. Dessler (1994), Numerical simulations of torus-driven plasma transport in the Jovian magnetosphere, *J. Geophys. Res.*, 99, 8755.

Young, D. T., *et al.* (2004), Cassini Plasma Spectrometer investigation, *Space Sci. Rev.*, 114, 1-112.

Young, D. T., et al. (2005), Composition and dynamics of plasma in Saturn's magnetosphere, *Science*, 307, 1262.